AWARD NUMBER: W81XWH-13-1-0442

TITLE: Targeting Ovarian Cancer with Porphysome Nanotechnology

PRINCIPAL INVESTIGATOR: Gang Zheng

CONTRACTING ORGANIZATION: University Health Network
Toronto, M5G 1Z5

REPORT DATE: October 2014

TYPE OF REPORT: Annual

PREPARED FOR: U.S. Army Medical Research and Materiel Command
Fort Detrick, Maryland 21702-5012

DISTRIBUTION STATEMENT: Approved for Public Release;
Distribution Unlimited

REPORT DOCUMENTATION PAGE

Form Approved
OMB No. 0704-0188

1. REPORT DATE	2. REPORT TYPE	3. DATES COVERED
October 2014	Annual	30Sep2013 - 29Sep2014

4. TITLE AND SUBTITLE

Targeting Ovarian Cancer with Porphysome Nanotechnology

5a. CONTRACT NUMBER

5b. GRANT NUMBER
W81XWH-13-1-0442

5c. PROGRAM ELEMENT NUMBER

6. AUTHOR(S)

Gang Zheng, Juan Chen

E-Mail: gang.zheng@uhnres.utoronto.ca

5d. PROJECT NUMBER

5e. TASK NUMBER

5f. WORK UNIT NUMBER

7. PERFORMING ORGANIZATION NAME(S) AND ADDRESS(ES)

University Health Network
200 Elizabeth Street
Toronto, ON, Canada
M5G 2C4

8. PERFORMING ORGANIZATION REPORT NUMBER

9. SPONSORING / MONITORING AGENCY NAME(S) AND ADDRESS(ES)

U.S. Army Medical Research and Materiel Command
Fort Detrick, Maryland 21702-5012

10. SPONSOR/MONITOR'S ACRONYM(S)

11. SPONSOR/MONITOR'S REPORT NUMBER(S)

12. DISTRIBUTION / AVAILABILITY STATEMENT

Approved for Public Release; Distribution Unlimited

13. SUPPLEMENTARY NOTES

14. ABSTRACT

Current conventional therapy includes surgery and chemotherapy has limitation for ovarian cancer (OC) management. OC remains the most lethal gynecologic malignancy and requires a novel therapeutics development to effectively change the current paradigm of care. Porphysomes with intrinsic multimodal biophotonic properties, favorable *in vivo* behaviors, and low toxicity, provide a multimodal imaging and therapeutic platform for OC management. In this project, we have developed a folate receptor (FR) targeted porphysome for potentially targeted OC management as FR expression has been reported in up to 90-95% of epithelial OC. We have demonstrated FR-mediated cell uptake of nanoparticles. After systematic administration to FR-positive tumor-bearing mice, the ^{64}Cu labeled FR-porphysome were capable to detect the tumor by PET imaging and NIR fluorescence imaging. In addition, FR-mediated delivery triggered nanostructure rapid disruption that ultimately restored the photodynamic reactivity of monomeric porphyrins which was quenched in the intact nanostructure, thus enabling selective and potent photodynamic therapy (PDT). To further improve the pharmacokinetics of FR-porphysome, we developed ultra-small porphyrin nanovehicle (PLP) with great biocompatibility, favorable pharmacokinetics, intrinsic multi-imaging modalities, potent PDT, and stable drug delivery functionalities. Therefore, PLPs provide a multimodal imaging and therapeutic platform that could enhance OC diagnosis by integrating PET/CT and fluorescence imaging, and improve OC therapeutic efficacy and specificity by tailoring treatment via fluorescence-guided surgical along with selective PDT, and potential chemotherapy. For Year 2, we plan to focus our efforts on the GMP-kit development for ^{64}Cu-porphysome to meet the Health Canada/FDA regulation for CTA filing, which will then be ready for the companion project (PI: A Oza) for Phase I clinical trials.

15. SUBJECT TERMS

Ovarian cancer, Folate receptor, Porphysome, Targeting therapy, Fluorescence imaging, PET/CT imaging, Photodynamic therapy, Porphyrin, Nanoparticles

16. SECURITY CLASSIFICATION OF:			17. LIMITATION OF ABSTRACT	18. NUMBER OF PAGES	19a. NAME OF RESPONSIBLE PERSON
					USAMRMC
a. REPORT	b. ABSTRACT	c. THIS PAGE			19b. TELEPHONE NUMBER *(include area code)*
Unclassified	Unclassified	Unclassified	Unclassified	40	

Table of Contents

Page

Introduction

More than 20,000 American women are diagnosed with ovarian cancer (OC) each year and most of these patients, diagnosis occurs when their disease has spread to surrounding tissue, rendering them with only 15-20% five-year survival. While current conventional therapy includes surgery and a limited range of chemotherapy, >75% of patient with stage III/IV disease will relapse and die because of developing drug resistance. Today, OC remains the most lethal gynecologic malignancy and a disease which requires an aggressive approach to novel therapeutics development—aligning expertise across the continuum of translational research to effectively change the current paradigm of care.

Porphysomes are the first-in-class all organic nanoparticles with intrinsic multimodal biophotonic properties. They are based on porphyrin-lipid building blocks that self-assemble into liposome-like nanoparticles (100-150nm diameter).[1] Due to its natural chlorophyll origin, porphyrin-lipid itself is biodegradable and has very low toxicity *in vivo* (1000 mg/kg *i.v.* in mice caused no detectable functional, hematological or histological effects). Prior to self-assembly, porphyrin-lipid is highly fluorescent. Upon self-assembly, the very high porphyrin packing density results in both 'super'-absorption and structure-dependent 'super'-quenching, which, in turn, converts light energy to heat with extremely high efficiency, giving them ideal photothermal and photoacoustic properties that are unprecedented for organic nanoparticles. Meanwhile, the aqueous core of porphysome can be actively or passively loaded with drugs. In addition, radioactive copper-64 (^{64}Cu) can be directly incorporated into the porphyrin-lipid building blocks of the preformed porphysomes to enable faithful tracking of the *in vivo* fate of the nanoparticle and its drug cargos.[2] Thus, the intrinsic multimodal nature of porphyrin-assembled nanoparticles confers high potential for cancer theranostics and clinical translation.

Unlike normal tissues, several human tumors overexpress the folate receptor (FR).[3] FR expression has been reported in up to 90-95% of epithelial OC and as such, development of folate as a potential single or combination targeted agent is of major interest and may be clinically relevant for OC management.[4] Symanowski et al., (2010) show the use of a folate-targeted imaging agent identifies patients with advanced OC most likely to benefit from folate-targeted therapy and suggest application of truly personalized medicine as it can be used to select and target a subgroup of patients most likely to respond to the therapy. Recently, findings from a phase II study in platinum-resistant OC have shown a twofold increase in progression-free survival when treated with pegylated liposomal doxorubicin (PLD); with strongest benefit in patients with FR-positive lesions—evidence that a sub-population of OC patients can be screened using companion FR-imaging agents.[5]

As such, we propose to use FR targeting for precise staging tumor, guiding tumor resection and delivering chemotherapy with our first-in-class, intrinsically multifunctional nanoparticle delivery system, called "porphysome", to optimize therapeutic specificity and efficacy.

Body

Aim 1: Preclinical Optimization & Validation of ^{64}Cu-FR-Porphysome for PET Imaging and Intraoperative Fluorescence Imaging in Clinically Relevant OC Models

1) Developing FR-targeted porphysome (FR-porphysome)

Folic acid is essential for rapid cell division and growth,[6] and binds folate receptor (FR) with high affinity ($K_d \sim 10^{-10}$ M).[7] Therefore, folate-conjugation has been applied to achieve active FR-targeting delivery of a broad range of theranostics and nanoparticles.[8, 9] We synthesized a model FR-targeting porphysome (FR-porphysome)[10] by including 1 mol% of folate-PEG2000-lipid (folate-lipid) in the porphysome formulation and compared its structure, photoactivities (fluorescence and singlet oxygen generation) and structure stability with that of the non-targeting porphysome (the previously reported regular porphysome). Like non-targeting porphysome, the FR-porphysome is spherical vesicle with size around 130 nm in diameter. (Appendix I, Figure 1), and produces 'super'-fluorescence quenching (over 99% quenching efficiency) when it is intact. The singlet oxygen production of the intact and the nanostructure-disrupted FR-porphysome were further examined and compared with that of non-targeting porphysome under PDT laser (671 nm) irradiation at a wide range of light doses (0.5-10 J/cm^2). As shown in Figure 1, both FR-porphysome and non-targeting porphysome displayed nanostructure-induced 'super'-quenching of singlet oxygen generation (over 90% of quenching efficiency) when compared with their corresponding nanostructure-disrupted samples. In addition, both non-targeting

porphysome and FR porphysome structures are highly stable either in buffer stock or in serum, evidenced by their fluorescence quenching remained after 24 h incubation in PBS buffer stock and 50% FBS at 37 °C. Taking together, these data demonstrated that the addition of folate-lipid in the particles formulation does not affect the nanostructure and photoproperties of porphysome.

2) Selective intracellular uptake of FR-porphysome

To validate the targeting specificity of FR-porphysome, the cellular uptakes of FR-porphysomes and non-targeting porphysome were examined in FR+ (KB) and FR- (HT1080) cells by measuring the unquenched porphyrin fluorescence signal in cell lysis buffer. The relative intracellular uptakes were normalized to the uptake of non-targeting porphysome in KB cells. As shown in Figure 2a, compared to non-targeting porphysomes that displayed similar low uptake in both cell lines, FR-porphysomes showed significantly enhanced (58.7-fold) uptake in FR positive KB cells after 3 h incubation, but much less enhanced (8.2 fold increase) uptake in FR low expression HT1080 cells. When increasing the incubation time from 3 h to 24 h, the uptake of non-targeting porphysome in both KB and HT1080 were negligibly increased (<0.5 fold), while the uptake of FR-porphysome were dramatically increased (172 fold) in KB cells (FR+) and slightly increased (24 fold) in HT1080 cells (FR-) (Figure 2b). In addition, the enhanced uptake of FR-porphysome in KB cells either for 3 h or 24 h incubation can be completely inhibited by free folic acid. These data demonstrated the specific FR-targeting enhanced intracellular uptake of FR-porphysome.

The FR-targeting triggered fluorescence activation was further assessed by confocal imaging. Although FR-porphysome showed efficient uptake in KB cells after 3 h incubation (Figure 2c), confocal imaging showed very weak fluorescence signal right after 3 h incubation, which indicated the FR-porphysome being intact nanostructure after initial internalization. Waiting for additional 21 h in regular cell culture condition, these cells showed much stronger porphyrin fluorescence (Figure 2d), suggesting that the disruption of FR-porphysome nanostructure in cells is a time-consuming process, which resulted in gradual unquenching of porphyrin photoproperties. The specific FR-mediated fluorescence activation of FR-porphysome was further validated by the effective inhibition using free folic acid (Figure 2d). In contrast, the control non-targeting porphysome did not show any fluorescence activation in cells at either 3 h right after incubation or 21 h later.

3) Validation of targeting-triggered PDT activation of FR-porphysome in FR+ cancer cells

To verify *in vitro* PDT activation of FR-porphysome after targeting-enhanced intracellular uptake, cell viability (MTT assay) was measured on the KB cells (FR+) with and without laser treatment. The cells treated with non-targeting porphysome were used as a control and the cell viability of each group was normalized to that of the untreated cells. As shown in Figure 3, neither non-targeting porphysome nor FR-porphysome had noticeable dark toxicity to cells at the porphyrin concentration of 5 μM. Upon PDT laser treatment (670 nm, 10 J/cm^2), non-targeting porphysome induced minor photocytotoxicity (96.4±8.5% of cell viability) while FR-porphysome decreased significantly the cell viability to 38.5±4.3%. Together with effective inhibition of the photocytotoxicity of FR-porphysome by extra free folic acid (93.1±7.4% of cell viability), these results suggested that the targeting-enhanced intracellular uptake and photoactivation of FR-porphysome ultimately resulted in significant improvement on PDT therapeutic outcomes.

4) *In vivo* fluorescence activation of FR-porphysome on KB tumor-bearing mice

Both fluorescence and singlet oxygen generation of porphyrin molecules are highly quenched in intact porphysomes, but are significantly activated when the nanostructure is disrupted. Therefore, fluorescence activation could serve as a useful indicator for assessment of the nanostructural disruption and singlet oxygen ($^1O_2$) activation. The *in vivo* fluorescence activation of the porphysomes was examined on KB-tumor bearing mice with intravenous administration of non-targeting or FR-porphysomes. As shown in Figure 4a, mice injected with FR-porphysome started to show fluorescence contrast in tumor over surrounding normal tissue as early as 6 h post-injection, while non-targeting porphysome did not display obvious fluorescence contrast in tumor area at that time point. After 24 h administration, tumor fluorescence increased significantly in FR-porphysome group, but was much weaker in non-targeting porphysome group. To investigate whether the FR-porphysomes giving enhanced fluorescence in tumor compared to non-targeting porphysomes is due to a higher tumor accumulation, we examined the tumor accumulation of two porphysomes by using radioisotope ^{64}Cu labelling procedure.[10] Surprisingly, we observed that the tumor accumulation of FR-porphysome was even

worse than that of non-targeting porphysome at either 6 h (4.4 ID%/g vs. 8.1ID%/g) or 24 h (3.1 ID%/g vs.7.6 ID%/g) (Figure 4b) post administration, indicating the enhanced fluorescence in tumor of FR-porphysome group was attributed by quicker fluorescence activation. All together, these data suggest that FR targeting significantly accelerated the *in vivo* fluorescence activation of porphysomes in tumor.

5) In vivo PDT efficacy of FR-porphysome

Non-targeting porphysome has been demonstrated as an efficient PTT agent upon high power laser irradiation (671nm, 750mW/cm^2).[11] We performed an *in vivo* PDT treatment here at much lower laser setting (671 nm, 150 mW/cm^2, 100 J/cm^2). The tumor temperature during the PDT treatment was monitored in real time by a thermal camera to ensure that the experimental laser treatment did not cause PTT effect. As shown in Figure 5a, no significant temperature increase (tumor temperature remained around 35 °C constantly) was observed for all laser treatment groups during the 10 min treatment, indicating that no PTT contribution was involved in the treatment. The PDT treatment efficacy was firstly evaluated by monitoring tumor growth rate. The tumor-bearing mice without any treatment served as blank control. As shown in the Figure 5b, the tumors received either the laser treatment or FR-porphysomes injection alone remained the same tumor growth trend as that of blank controls, indicating that neither PDT laser nor FR-porphysome induced any therapeutic effect. FR-porphysome plus PDT laser completely inhibited the tumor growth, while non-targeting porphysomes plus PDT laser negligibly decrease the tumor growth, which demonstrated the folate-targeting triggered photodynamic activation of porphysomes in tumor.

The mice survival study was further conducted after treatment (Figure 5c). For the groups (n=5/group) of blank control, PDT laser alone and FR-porphysome alone, tumors appeared unaffected and grow continuingly (Figure 5d) to reach the end point completely at day 12, 10 and 12, respectively (Figure 5c). For the mice received non-targeting porphysome plus laser, no obvious tumor ablation was observed after treatment (Figure 5d) and the tumors started to reach the end point at day 4 (80 %) post-PDT treatment and ended completely at day 13 post PDT (Figure 5c). For the animals treated with FR-porphysome plus laser, the treated tumor tissue became swollen at day 2 post PDT, displayed dark brown ablation from day 3 post-PDT (Figure 5d), and the tissues slowly recovered in the following two weeks with 80% survival rate (Figure 5c). To further investigate the PDT response on the cellular level, another set of treatment groups were scarified at 24 h post-PDT and the tumors and some normal organs, including tumor surrounding muscles, livers, kidneys, and spleens, were harvested for H&E histology analysis (Figure 6). As expected, only the tumor from the mice received FR-porphysome plus laser showed clear cellular damage while the tumors from other groups did not, which confirmed the specific FR-porphysome-enabled PDT efficacy. In addition, no obvious cellular damage and morphology change were observed in the collected normal organs for all treatment groups when compared to that of non-treated blank control, indicating that the FR-porphysome-enabled PDT is a safe treatment procedure.

In summary, the less uptake of FR-porphysome in tumor resulted in more efficient photodynamic activation in tumor when compared to non-targeting porphysome. The explanation could be that FR-porphysome was actively delivered into tumor cells to undergo efficient photodynamic activation and achieve efficient therapeutic outcomes. Whereas non-targeting porphysome showed a higher uptake in tumor, but mostly accumulated in the interstitial space through EPR effect, thus PDT remains inactive upon treatment. The contradiction of accumulation and treatment efficacy for non-targeting porphysome and FR-porphysome strongly supports the targeting-triggered PDT activation of porphysome.

6) Developing ultra-small size of porphyrin nanovehicle to improve *in vivo* pharmacokinetics of FR-porphysome

It is somewhat surprising that the accumulation of ^{64}Cu-FR-porphysome in tumor was relatively lower than that of non-targeting ^{64}Cu-porphysome (4.4 ID%/g *vs* 8.1ID%/g and 3.1 ID%/g *vs* 7.6 ID%/g at 6 h and 24 h post administration, respectively, Figure 4b). For nanoparticles with size around 100 nm, enhanced permeability and retention (EPR) effect usually dominates their tumor accumulation. A prolonged circulation time would facilitate the filtration of nanoparticles from the blood circulation directly into the tissues and enhance the retention of the particles in the diseased area. By investigating the pharmacokinetics of these particles, we found that FR-porphysome has much shorter blood circulation half-life (<4 h) than non-targeting porphysome (10 h) (Figure 7), which could explain the lower accumulation of FR-porphysome in tumor.

Recent studies have demonstrated that nanoparticles less than 40 nm displayed more effective at penetrating deeply into fibrous tumors than their larger counterparts.[12-14] We recently also developed a sub-40 nm porphyrin lipid nanodisc and demonstrated the small size nanodiscs displayed a 5-fold increase of diffusion coefficient in comparison to the larger size porphysomes (130nm), in diffusing through a tumor's collagen-rich matrix.[15] Therefore, decreasing the size of porphysome might enhance its tumor accumulation. However, attempts to create smaller porphysome by the self-assembly of phophyrin-lipid remain a challenge due to growing instability as a result of the surface curvature.

We created ultra-small size of porphyrin nanovehicle (PLP) by assembly of phospholipid monolayer of porphyrin lipid with DMPC on a hydrophobic core of cholesteryl oleate, in aqueous buffered solution, followed by size-constraint with an 18-amino acid ApoA-1 mimetic peptide (Appendix II). We found the structural and photophysical properties of the PLP are dependent on the ratio of porphyrin-lipid to DMPC. As shown in Figure 8a, increasing the ratio of porphyrin lipid to DMPC led to the enhanced porphyrin fluorescence quenching and increased particles size. When the ratio was over 30%, high fluorescence quenching (>95%) was achieved and the particles size was still controlled under 30nm. The PLP with 30% mol porphyrin-lipid/70% mol of DMPC was chosen as an optimal PLP for further application studies, as it contained the maximum porphyrin lipid for a stable and monodisperse PLP, had favorable size (<30nm, Figure 8b), and exhibited efficient fluorescence quenching. Based on the absorbance spectrum of pyropheophorbide-lipid, the estimated PLP extinction coefficient ε680 was 7.8×10^7 $cm^{-1}M^{-1}$. This enhanced light absorption indicates the high density of porphyrin environment in PLP. The circular dichroism (CD) spectrum of PLP confirmed the alpha helix structure of PLP (Figure 8c).

The optical properties of PLPs were similar to that observed for porphysomes, the high density of porphyrin environment extremely inhibited the fluorescence generation and the singlet oxygen production of PLP (Figure 8e, f). The fluorescence of PLP was quenched by 100 fold when compared with the nanostructure-disrupted samples. Upon PDT laser (671 nm) irradiation at a wide range of light fluence (0.5-10 J/cm^2), PLPs exhibited 2-3 fold less singlet oxygen generation when compared with the nanostructure-disrupted samples. Therefore, the intact PLP is photodynamic inactive, while it will become PDT active when the nanostructure is disrupted.

The pharmacokinetics profile of PLPs was examined on healthy mice (Figure 9). Three groups were compared in the study: PLP, PEG-PLP (PEGylated PLP) and active targeting FR-PLP (folate receptor-targeted PLP). As shown in Figure 9, regardless of PEGylation, both PLP and PEG-PLP had similar and favorable circulation slow half-life (9.9 h for PLP and 9.5 h for PLP-PEG, respectively), indicating no need of PEGylation for improving in vivo circulation, whereas PEGylation is essential for porphysomes structure to ameliorate their stability *in vivo*. Interestingly, in contradictory to our previous observation that the involvement of folate-lipid in porphysome formulation shortened the particle in vivo circulation time, FR-PLP exhibited a significantly prolonged slow half-life (13.3 h for folate-PLPs *vs* < 4h for FR-porphysomes). We believe this prolonged circulation would benefit the infiltration of nanoparticles from the blood circulation directly into the tissues and enhance the retention of the particles in the targeting diseased area. Thus, more efficient targeting delivery and more effective photoproperties (fluorescence and singlet oxygen generation) activation would be expected for FR-PLP in FR-positive cancer types comparing to FR-porphysomes.

We further demonstrated this smaller particles size advantage for *in vivo* delivery on a 9Lluc glioma mouse model. Mice with 9Lluc glioma were injected with PLP (21 nm) and porphysome (130 nm) at the porphyrin concentration of 200 nmol, and the mice crania were removed under anesthesia at 24 h post-administration to expose the tumors for fluorescence images *in situ*. As shown in Figure 10a, the middle column, both PLP and porphysome can delineate clearly the tumor from the surrounding healthy brain by fluorescence imaging which well-matched with the tumor sites defined by BLI imaging (Figure 10a, left column). However, the fluorescence signal from the PLP-administrated tumor was much stronger than that of the porphysome-dosed one, suggesting the benefit of the ultra-small PLPs (<30nm) on enhancing tumor-specific accumulation. The specificity of tumor accumulation of PLP in 9Lluc glioma tumor was further demonstrated by *ex vivo* brain tissue imaging (Figure 10b), where the fluorescent core in brain marched well with the tumor region depicted by H&E histology slice. We further validated the tumor-specific uptake of PLP at microscopic level using confocal imaging of the frozen brain tissue slice, where strong porphyrin signal was observed only in tumor peripheral region, but not in contralateral brain area (Figure 10c).

We investigated extensively the potential application of PLP for PDT *in vivo*. The fluorescence activation of PLP could serve as a useful indicator for assessment of the nanostructural disruption and singlet oxygen activation. For example, we investigated PDT efficacy of in glioma tumor. Four groups, including blank control, laser control, PLP control and PLP-PDT (PLP + Laser) group, were employed to evaluate the PDT efficacy of PLP. At 24 h post-injection, PLP-PDT group was subjected to trans-cranium laser irradiation (671 nm, 50 mW/cm^2, 50 J/cm^2) Minimal temperature increase during the treatment excluded the thermal effect. The PDT efficacy was evaluated by post-mortem histopathological analysis. PLP-PDT group displayed condensed nuclei and loss of cell structure in tumor while control groups did not (Figure 11a). TUNEL staining analysis further revealed that PLP-PDT induced significant tumor cell apoptosis (67.5 ± 11.4 %), while the controls showed minimal tumor apoptosis (1.77 ± 1.37% for blank, 0.17 ± 0.05 % for laser control and 0.19 ± 0.07 % for PLP control) (Figure 11b). Moreover, the adjacent healthy brain after PLP-PDT show none of cellular damage, morphology change and cell apoptosis, demonstrating the high selectivity of PLP-PDT to tumors. Therefore, PLP enable tumor-specific PDT at very low light dose while preservation of normal health, thus providing a safe PDT treatment protocol.

As PLP has a core-shell nanostructure with a hydrophobic core surrounded by lipid monolayer, it has amiable potential for loading and safe delivery of hydrophobic bioactive compounds. In this study, a near-infrared fluorescent hydrophobic dye, DiR-BOA, was used as a drug surrogate to examine the drug loading capacity and delivery behaviors of PLP. By adding 0.5 mol of DiR-BOA in the PLP formulation (0.9 μmol porphyrin-lipid, 2.1 μmol DMPC and 0.3 μmol CO), DiR-BOA was successfully loaded into the particle with loading efficiency of 85%. The resulted PLP (DiR-BOA) with size of 22.5 nm was quite stable in PBS at 4 °C, as minimal size change and negligible DiRBOA leakage were observed over 30 days. We then investigated the *in viv*o behaviours of the PLP (DiR-BOA) in orthotopic U87 glioma bearing mice. The mice after 24 h injection of PLP (DiR-BOA) were subjected to the crania removal surgery under anesthesia, and fluorescence imaged at porphyrin channel (Ex: 615 nm, Em: 680-750nm) and NIR drug surrogate channel (Ex: 750 nm, Em: 780-950), respectively, using CRI MaestroTM imaging system. As shown in Figure 12a, both porphyrin and DiR-BOA signals were highly concentrated in the tumor, which clearly delineated tumor margin while sparing healthy brains close-by. In addition, these two fluorescence signals were well-colocalized, suggesting that the PLP (DiR-BOA) enable a stable and efficient delivery of drug surrogate selectively in tumor. More interestingly, this highly efficient delivery allowed for fluorescence detection of tumor cells at microscopic level by an *in vivo* fluorescence confocal microscopy with a deep-red long-pass filter, while sparing non-fluorescent contralateral brain cells (Figure 12b). To further validate the tumor-specific accumulation of PLP, its tissue biodistribution was examined by fluorescence imaging when the animals were sacrificed. As shown in Figure 12c, only glioma tumor and liver exhibited strong fluorescence signals of porphyrin and DiR-BOA, while other organs showed negligible fluorescence, demonstrating an extremely high tumor-specific uptake of PLP(DiR-BOA). Similar to most nanoparticle's delivery, the high liver uptake of PLP was probably due to their hepatobillary clearance. But unlike most nanoparticle's delivery including porphysomes, a much lower spleen uptake of PLP was probably benefited from its ultra-small size that contributed to the 'escape' from filtering-out by the reticuloendothelial system. The well-correlation between the porphyrin fluorescence and DiR-BOA fluorescence in all of the detected tissues (Figure 12c) further demonstrated the structural intact of PLP(DiRBOA) in systemic delivery to accumulation in various tissues. Altogether, these data suggested that 1) the PLP provides a highly tumor selective and efficient drug delivery system for cancer therapy with minimal pre-leakage and off-target effect; 2) due to the stable delivery characters, the porphyrin signal of PLP, such as fluorescence, could be used for tracking drug delivery to guide the treatment planning.

7) PET Imaging and Intraoperative Fluorescence Imaging in Clinically Relevant OC Models

Finally, we successfully incorporated ^{64}Cu into the preformed PLP with high ^{64}Cu labelling efficiency (>95%) and followed by investigation of its delivery behaviors. As shown in Figure 13, ^{64}Cu-PLP enabled selectively picking up ovarian cancer metastases, where metastases tumors exhibited super bright PET signal while the surrounding tissue, such as fallopian tube, showed minimal signal. The PET imaging-enabled tumor-specific picking up was further confirmed by *ex vivo* tissue porphyrin fluorescence imaging, which was well-correlated with the bioluminescence signal from tumor cells. The metastases tissue was further identified by histology analysis. Thus, the intrinsically ^{64}Cu labelling of PLP enable non-invasive and accurate tracking the

nanoparticles delivery and additionally detect tumor due to its tumor-preferential accumulation, thus showing great promise for translation to clinical application.

Key Research Accomplishments:

- Developed a folate receptor targeted porphysome (FR-porphysome) and ^{64}Cu-FR-porphysome for targeting PET imaging of tumor on mouse model.
- Demonstrated the FR-mediated cell uptake of FR-porphysome, which resulted in rapid nanostructure disruption in cells and ultimately triggered the unquenching of porphyrin fluorescence as well as singlet oxygen generation for low background fluorescence imaging and highly selective PDT.
- To further improve the pharmacokinetics of FR-porphysome, we have developed an ultra-small size porphyrin nanovehicle (PLP) and demonstrated that it has similar optical properties as porphysome (the high density of porphyrin environment extremely inhibited the fluorescence generation and the singlet oxygen production of monomeric porphyrins), but exhibits a significantly prolonged half-life in blood circulation (13.3 h for FR-PLPs *vs* < 4h for FR-porphysomes).
- PLP allows for rapid nanostructure dissociation upon tumor accumulation to release monomeric porphyrins to generate efficiently fluorescence and photodynamic reactivity which are highly-silenced in intact PLP, thus providing an activatable mechanism for low-background NIR flurescence imaging.
- PLP provides capability for stable drug loading and delivery.
- The successful chelation of ^{64}Cu in PLP enabled PET imaging of ovarian cancer metastases on mouse model.
- This set the stage for the Year 2 plan of a GMP-kit development for 64Cu-porphysome to meet the Health Canada/FDA regulation for CTA filing, which will then be ready for the companion project (PI: A Oza) for Phase I clinical trials.

Reportable Outcomes:

- Manuscript: Cui L, Lin Q, Jin CS, Jiang W, Huang H, Ding L, Muhanna N, Irish JC, Wang F, Chen J, Zheng G.A PEGylation-Free Biomimetic Porphyrin Nanoplatform for Personalized Cancer Theranostics. ACS Nano. 2015, 9: 4484-95.
- Manuscript: Jin CS, Cui L, Wang F, Chen J, Zheng G. Targeting-triggered porphysome nanostructure disruption for activatable photodynamic therapy. Adv Healthc Mater. 2014, 3:1240-9.
- Manuscript: Liu TW, Stewart JM, Macdonald TD, Chen J, Clarke B, Shi J, Wilson BC, Neel BG, Zheng G. Biologically-targeted detection of primary and micro-metastatic ovarian cancer. Theranostics, 2013, 3:420-7.
- Abstract: Cui L, Lin Q, Jiang W, Ding L, Chen J, Zheng G, Porphyrin-lipid assembled HDL-like nanovesicles for fluorescence imaging and PDT treatment of orthotopic tumor. Poster presentation, International Conference on Porphyrins and Phthalocyanines (ICPP 8), Istanbul, Turkey, June 21st to June 27nd, 2014.
- Abstract: Cui L, Lin Q, Jiang W, Ding L, Chen J, Zheng G, Porphyrin-lipid assembled HDL-like nanovesicles for fluorescence imaging and PDT treatment of orthotopic tumor. Biomedical Optics (BIOMED) by OSA, Miami, April 26th to April 28nd, 2014.
- Abstract: Cui L, Ng Ken, Dave N, Chen J, Zheng G, Porphyrin-based built-in sensot for imaging liposomal nanoparticles integrity and drug delivery, Poster presentation, World Molecular Imaging Confess (WMIC), Savannah, Georgia, Sept 18th to Sept 21th, 2103.

- Abstract: Jin C.S., Chen J., Zheng G., Porphyrin-based Nanostructure-dependent Phototherapy: a closed loop between photodynamic and photothermal therapy. 2014 International Conference on Porphyrins and Phthalocyanines (ICPP 8), Istanbul, Turkey, June 21st to June 27nd, 2014.
- Abstract: Jin C.S., Chen J., Zheng G., Porphyrin-based Nanostructure-dependent Phototherapy: a closed loop between photodynamic and photothermal therapy. Biomedical Optics (BIOMED) by OSA, Miami, April 26th to April 28nd, 2014.
- Abstract: Jin CS, Anayama T, McVeigh P, Nakajima T, Wilson, BC, Yasufuku K, Zheng G. Porphysome-enabled Fluorescence-guided Photothermal Therapy to Treat Lung Cancer: a Pre-clinical Study in Rabbit Orthotopic Lung Tumor Model. World Molecular Imaging Confess (WMIC), Savannah, Georgia, Sept 18th to Sept 21th, 2103.

Conclusion:

FR-porphysomes has been developed by incorporating a small molar percentage of folate conjugate lipid in porphysome formulation. After systematically administrated to FR-positive tumor-bearing mice, the ^{64}Cu labelled FR-porphysome were capable to detect the tumor by PET imaging and NIR fluorescence imaging. Additionally, FR receptor targeting facilitated nanostructure rapid disruption inside the targeted cells to ultimately trigger the unquenching of porphyrin fluorescence as well as singlet oxygen generation, allowing low background fluorescence imaging and selective PDT upon laser irradiation. To further improve the pharmacokinetics of FR-porphysome, we developed ultra-small porphyrin nanovehicle (PLP) with great biocompatibility and *in vivo* behaviors. PLP exhibited intrinsically multimodal imaging and therapeutic functionalities. Its inherent activatable NIR fluorescence and metal chelation enabled PET imaging provided comprehensive information for early diagnosis, disease staging, intraoperative guidance, and quantitative assessment of drug delivery. Together with the potent PDT competency, PLP allowed for the tuning of patient treatment *vi*a imaging-guided surgery, effective PDT and potential chemotherapeutics delivery. For Year 2, we plan to focus our efforts on the GMP-kit development for ^{64}Cu-porphysome to meet the Health Canada/FDA regulation for CTA filing, which will then be ready for the companion project (PI: A Oza) for Phase I clinical trials.

References

1. Lovell, J. F.; Jin, C. S.; Huynh, E.; Jin, H.; Kim, C.; Rubinstein, J. L.; Chan, W. C.; Cao, W.; Wang, L. V.; Zheng, G. Porphysome Nanovesicles Generated by Porphyrin Bilayers for Use as Multimodal Biophotonic Contrast Agents. *Nature materials* 2011, 10, 324-332.
2. Liu, T. W.; Macdonald, T. D.; Jin, C. S.; Gold, J. M.; Bristow, R. G.; Wilson, B. C.; Zheng, G. Inherently Multimodal Nanoparticle-Driven Tracking and Real-Time Delineation of Orthotopic Prostate Tumors and Micrometastases. *ACS nano* 2013, 7, 4221-4232.
3. Kamen, B. A.; Smith, A. K. A Review of Folate Receptor Alpha Cycling and 5-Methyltetrahydrofolate Accumulation with an Emphasis on Cell Models in Vitro. *Advanced drug delivery reviews* 2004, 56, 1085-1097.
4. Kalli, K. R.; Oberg, A. L.; Keeney, G. L.; Christianson, T. J.; Low, P. S.; Knutson, K. L.; Hartmann, L. C. Folate Receptor Alpha as a Tumor Target in Epithelial Ovarian Cancer. *Gynecologic oncology* 2008, 108, 619-626.
5. van Dam, G. M.; Themelis, G.; Crane, L. M.; Harlaar, N. J.; Pleijhuis, R. G.; Kelder, W.; Sarantopoulos, A.; de Jong, J. S.; Arts, H. J.; van der Zee, A. G.; Bart, J.; Low, P. S.; Ntziachristos, V. Intraoperative Tumor-Specific Fluorescence Imaging in Ovarian Cancer by Folate Receptor-Alpha Targeting: First in-Human Results. *Nature medicine* 2011, 17, 1315-1319.
6. Antony, A. C. The Biological Chemistry of Folate Receptors. *Blood* 1992, 79, 2807-2820.
7. Sudimack, J.; Lee, R. J. Targeted Drug Delivery Via the Folate Receptor. *Advanced drug delivery reviews* 2000, 41, 147-162.
8. Paulos, C. M.; Turk, M. J.; Breur, G. J.; Low, P. S. Folate Receptor-Mediated Targeting of Therapeutic and Imaging Agents to Activated Macrophages in Rheumatoid Arthritis. *Advanced drug delivery reviews* 2004, 56, 1205-1217.
9. Turk, M. J.; Waters, D. J.; Low, P. S. Folate-Conjugated Liposomes Preferentially Target Macrophages Associated with Ovarian Carcinoma. *Cancer letters* 2004, 213, 165-172.
10. Jin, C. S.; Cui, L.; Wang, F.; Chen, J.; Zheng, G. Targeting-Triggered Porphysome Nanostructure Disruption for Activatable Photodynamic Therapy. *Advanced healthcare materials* 2014, 3, 1240-1249.
11. Jin, C. S.; Lovell, J. F.; Chen, J.; Zheng, G. Ablation of Hypoxic Tumors with Dose-Equivalent Photothermal, but Not Photodynamic, Therapy Using a Nanostructured Porphyrin Assembly. *ACS nano* 2013, 7, 2541-2550.
12. Cabral, H.; Matsumoto, Y.; Mizuno, K.; Chen, Q.; Murakami, M.; Kimura, M.; Terada, Y.; Kano, M. R.; Miyazono, K.; Uesaka, M.; Nishiyama, N.; Kataoka, K. Accumulation of Sub-100 Nm Polymeric Micelles in Poorly Permeable Tumours Depends on Size. *Nature nanotechnology* 2011, 6, 815-823.
13. Pluen, A.; Boucher, Y.; Ramanujan, S.; McKee, T. D.; Gohongi, T.; di Tomaso, E.; Brown, E. B.; Izumi, Y.; Campbell, R. B.; Berk, D. A.; Jain, R. K. Role of Tumor-Host Interactions in Interstitial Diffusion of Macromolecules: Cranial Vs. Subcutaneous Tumors. *Proceedings of the National Academy of Sciences of the United States of America* 2001, 98, 4628-4633.
14. Sykes, E. A.; Chen, J.; Zheng, G.; Chan, W. C. Investigating the Impact of Nanoparticle Size on Active and Passive Tumor Targeting Efficiency. *ACS nano* 2014, 8, 5696-5706.
15. Ng, K. K.; Lovell, J. F.; Vedadi, A.; Hajian, T.; Zheng, G. Self-Assembled Porphyrin Nanodiscs with Structure-Dependent Activation for Phototherapy and Photodiagnostic Applications. *ACS nano* 2013, 7, 3484-3490.

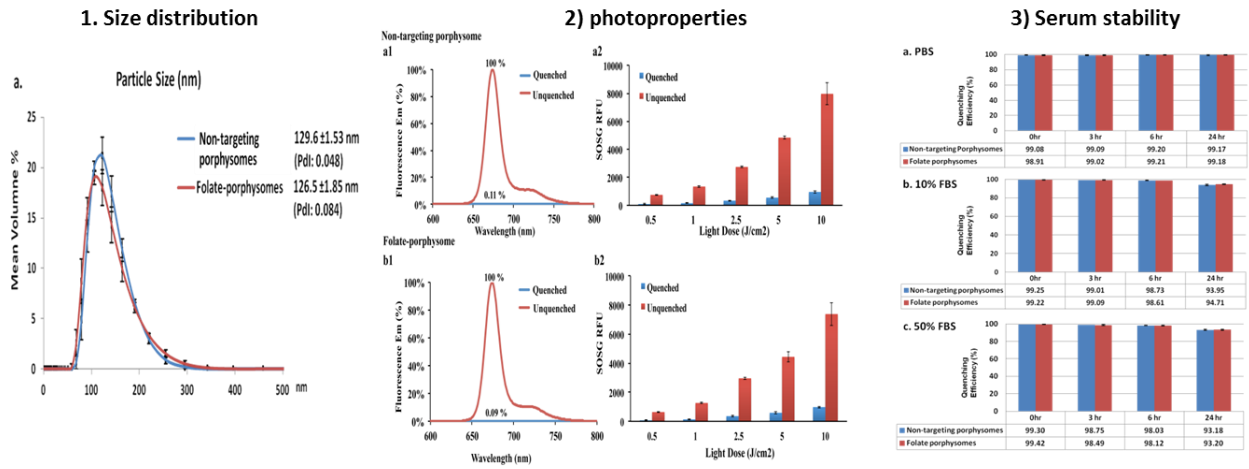

Figure 1. 1) particle sizes of non-targeting porphysomes and folate porphysomes (FR-porphysome). 2) The characterization of fluorescence and singlet oxygen generation of porphysomes. a1) Fluorescence emission of intact (quenched) versus disrupted non-targeting porphysomes (unquenched). a2) Singlet oxygen generation reported by SOSG fluorescence intensity upon laser irradiation (671nm, 50mWcm^{-2}) for intact versus disrupted porphysomes at light dose from 0.5 to 10 J cm^{-2}. b1) Fluorescence emission of intact (quenched) versus disrupted FR-porphysomes (unquenched). b2) Singlet oxygen generation reported by SOSG fluorescence intensity upon laser irradiation (671 nm, 50 mW cm^{-2}) for intact versus disrupted FR-porphysomes at light dose from 0.5 to 10 J cm^{-2}. 3) The stability of porphysomes in a, PBS; b, 10% FBS; c, 50% FBS after 3 h, 6 h and 24 h incubation. Data expressed as mean ± S.D. (n=3). The fluorescence quenching efficiency for each sample was calculated by comparing their fluorescence intensity with the corresponding unquenched samples (non-targeting porphysome) or FR-porphysome in 1% Triton solution).

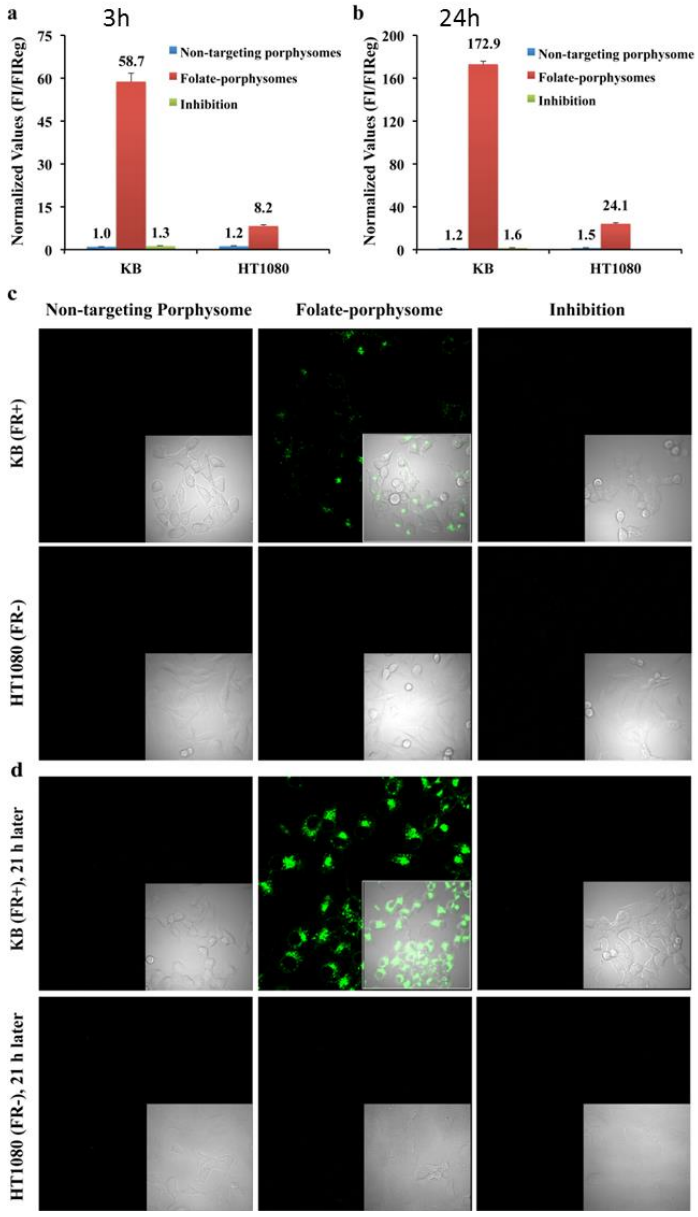

Figure 2. Quantitative cellular uptake and fluorescence activation of non-targeting porphysome, FR-porphysome, and FR-porphysome with folic acid inhibition in KB cells (FR+) and HT1080 cells (FR−). Intracellular uptakes were quantified by measuring porphyrin fluorescence signal in cell lysis buffer at a) 3 h and b) 24 h incubation of porphysome samples. The relative intracellular uptakes were normalized to the uptake of nontargeting porphysome in KB cells. The confocal fluorescence imaging of the KB and HT1080 cells (c) right after 3 h incubation and (d) 21 h post 3 h incubation with non-targeting porphysomes, FR-porphysomes, and FR-porphysomes with free folic acid (porphyrin concentration: 5×10^{-6} M).

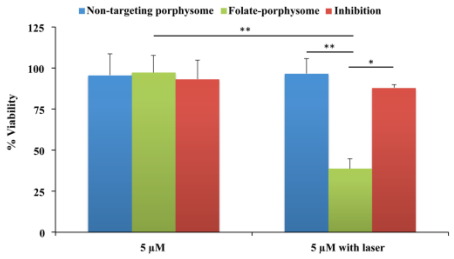

Figure 3. The targeting-triggered PDT activation of porphysome was investigated by measuring the cell viability with and without laser treatment using MTT assay. PDT treatment method: 671 nm laser at 10 J cm^{-2}. Cell viability was normalized to that of the untreated cells.

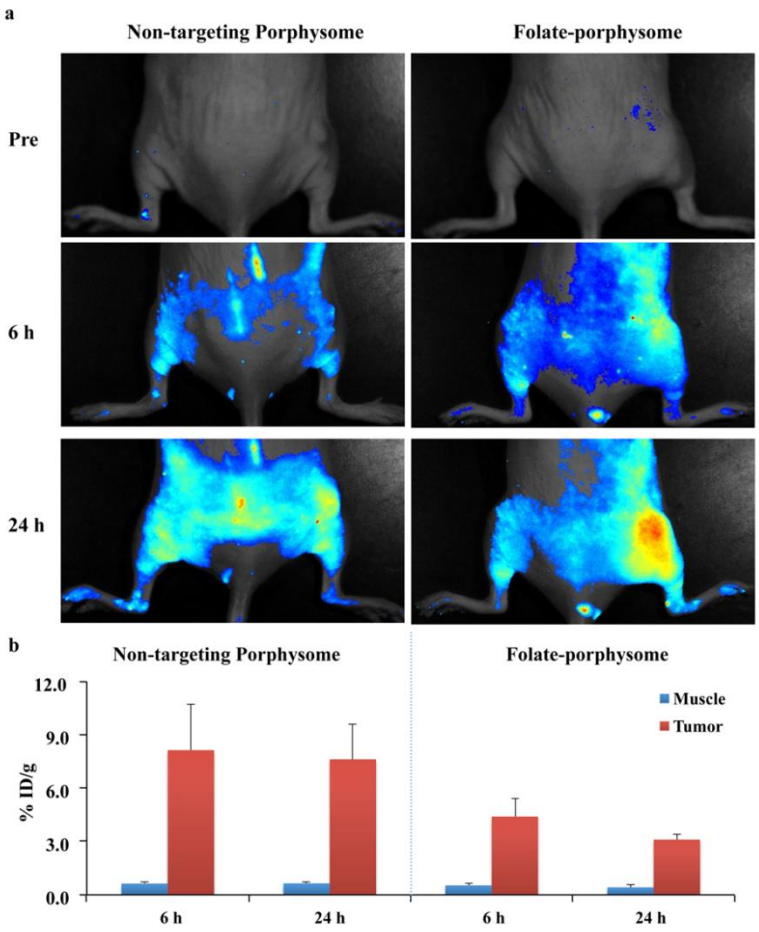

Figure 4. *In vivo* fluorescence activation and quantification of uptake in tumor versus muscle in KB-tumor-bearing mice. a) Fluorescence image of animals at pre-injection, 6 and 24 h-post *i.v.* injection of non-targeting and FR-porphysomes with a dose of 10 mg/kg. b) Accumulation of ^{64}Cu-labeled porphysomes in muscle and tumor at 6 h and 24 h post-injection were quantified by (γ-counting approach, plotted as % injected dose/gram (%ID/g). (n = 4)

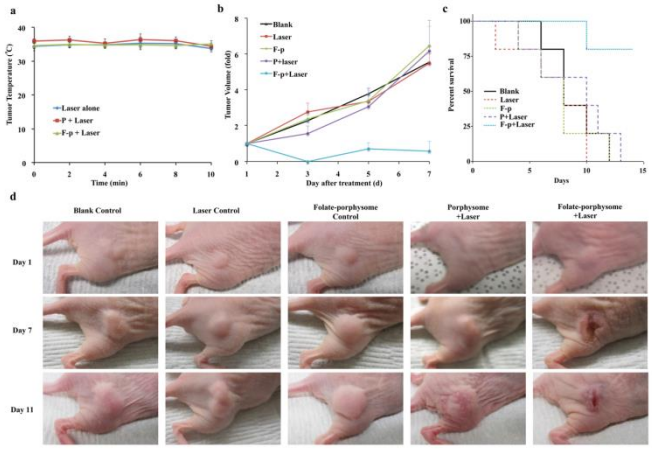

Figure 5. In vivo PDT treatment response in KB-tumor bearing mice. Mice were injected with non-targeting and FR-porphysomes at a dose of 10mg.kg^{-1}. a) Real-time monitoring of tumor temperature during 10 min laser irradiation. b) Tumor growth curve after treatment for each group (n = 5). c) Survival curve of animals after treatment for each group (n = 5). d) Representative mice tumor images at day 1, day 7, and day 14 post PDT treatment.

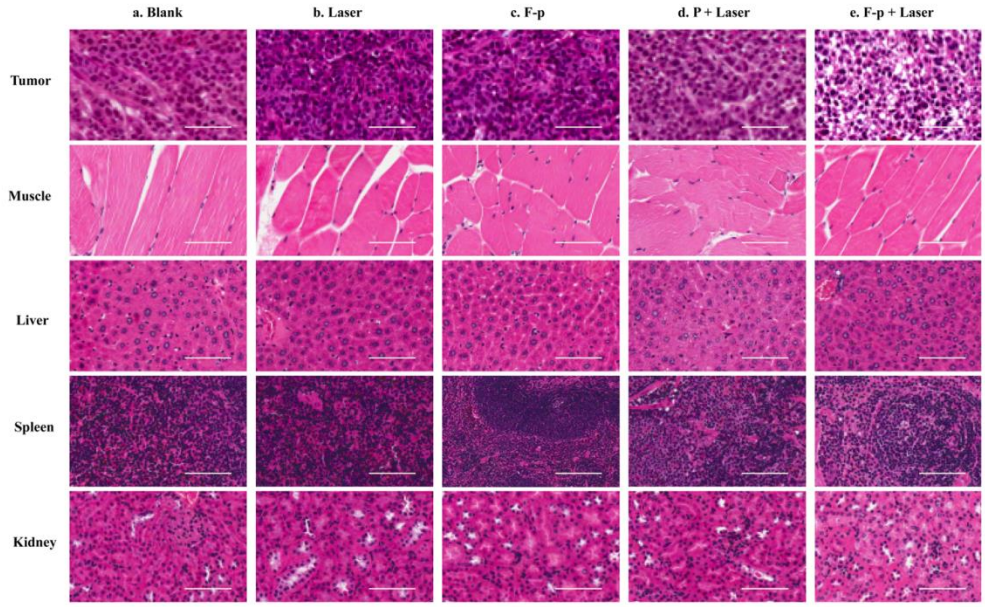

Figure 6. H&E staining of tumor, surrounding muscle, liver, spleen, and kidney tissue slices for different groups: blank control, laser alone, FR-porphysome(F-p), non-targeting porphysome plus laser (P+laser), and FR-porphysome plus laser (F-p+laser), at 24 h post PDT treatment.

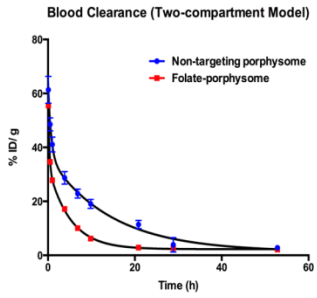

	Non-targeting-porphysome	Folate-porphysome
Half Life (Slow)	10.36	3.50
Half Life (Fast)	0.47	0.18
R^2	0.9825	0.9807

Figure 7. Blood clearance curve. Non-targeting and FR-porphysomes were *i.v.* injected to BALB/c mice at the dose of 10 mg/kg (n=4). Blood was collected from the leg vein of the mice serially prior to and after the injection (5 min, 30 min, 1 h, 3h, 6 h, 9 h, 11h, 24 h, 48 h and 72 h). Blood were placed at room temperature for 30 min to separate plasma, and then centrifuged for 10 min at the rate of 12,000 rpm. The fluorescence of the supernatant was measured by Spectrofluorometer (HORIBA Scientific Inc.) to calculate the porphyrin amount in the blood (Excitation 420 nm, Emission, 675 nm, Slit width: 2 nm). The porphyrin amount at each time point was then analyzed by Graphpad Prism® to calculate half-life of non-targeting porphysome and FR-porphysome.

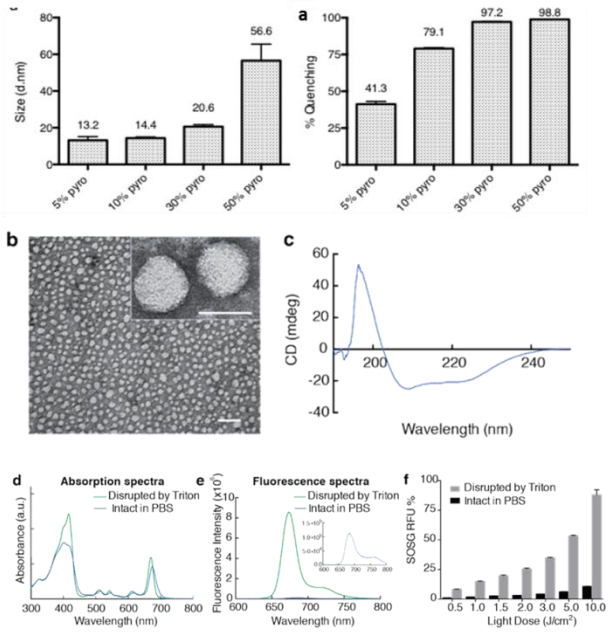

Figure 8. a. Sizes in diameter (volume distribution peak) and porphyrin fluorescence quenching efficiency of formulations with various pyro initial input (pyrolipid/total phospholipid= 5%, 10%, 30% and 50%) Porphyrin fluorescence quenching % = $(1- FI_{intact\ in\ PBS}/FI_{disrupted\ in\ Triton})\times 100\%$. b. TEM showed a core-shell spherical structure of PLP with size around 20 nm (the scales represented 100 nm and 20 nm respectively, for the whole view and the magnified view).c. Circular dichroism spectrum of PLP, affirming the α-helix structure assembled on the particle. d. UV-Vis absorption spectra of intact (blue) and nanostructure-disrupted (green) PLPs. e. Fluorescence emission spectra of intact (blue) and disrupted (green) PLPs. f. Singlet oxygen generation of intact and disrupted PLP upon laser irradiation at light dose from 0.5 J/cm^2 to 10 J/cm^2 measured by singlet oxygen sensor green (SOSG) assay.

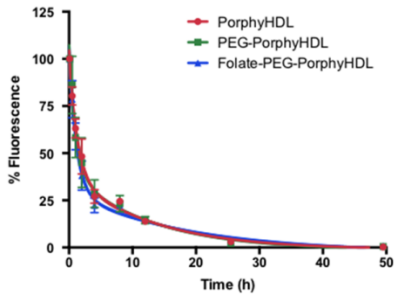

	PLP	PEG-PLP	FR-PLP
Slow Half Life (h)	9.877	9.515	13.27
Fast Half Life (h)	0.9714	0.8780	0.8749
R square	0.9825	0.9545	0.9748

Figure 9. Blood clearance profile of PLP, PEG-PLP and FR-PLP.

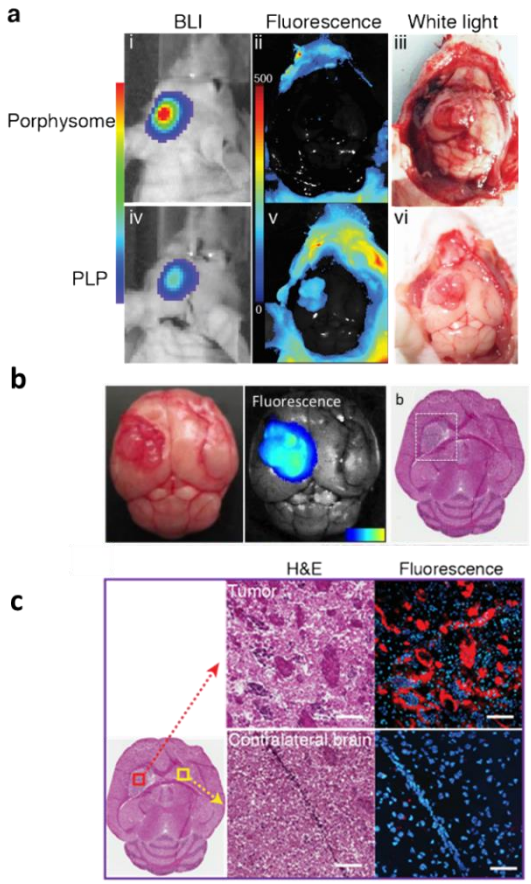

Figure 10. Tumor-specific accumulation of PLP in glioma. a. intra-operative bioluminescence, fluorescence and white light images of 9Lluc glioma-bearing mice under the crania opening after 24 h injection of porphysomes and PLP. b. (a) White image (left), *ex vivo* fluorescence image (middle) and H&E staining image (right) of the brain from 9Lluc mouse with PLP-administration. c) Representative H&E staining image of brain from PLP-administrated mice, with the magnified images showed the corresponding H&E staining and fluorescence microscopic imaging (blue: DAPI, red: porphyrin) of the tumor region and contralateral healthy brain region (scale bar: 100 μm).

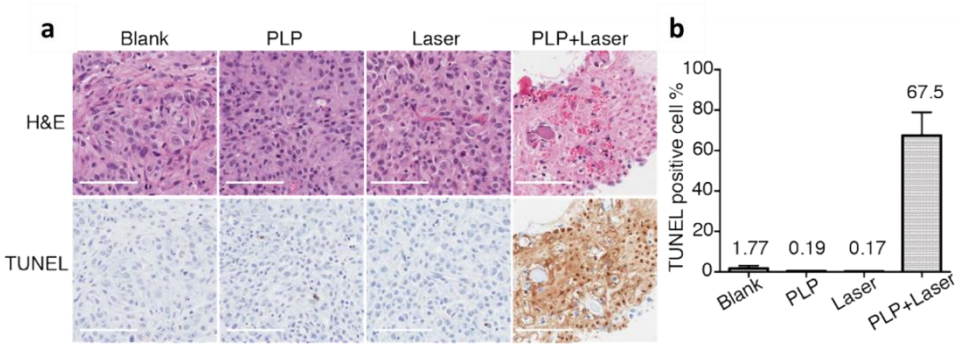

Figure 11. Representative H&E and TUNEL staining of glioma tumor sections from the blank control, laser alone control, PLP alone control and PLP-PDT group at 24 h post-PDT (scale bar: 100 μm). d. Quantitative analysis of TUNEL positivity out of whole tumor region in the four groups (n=3).

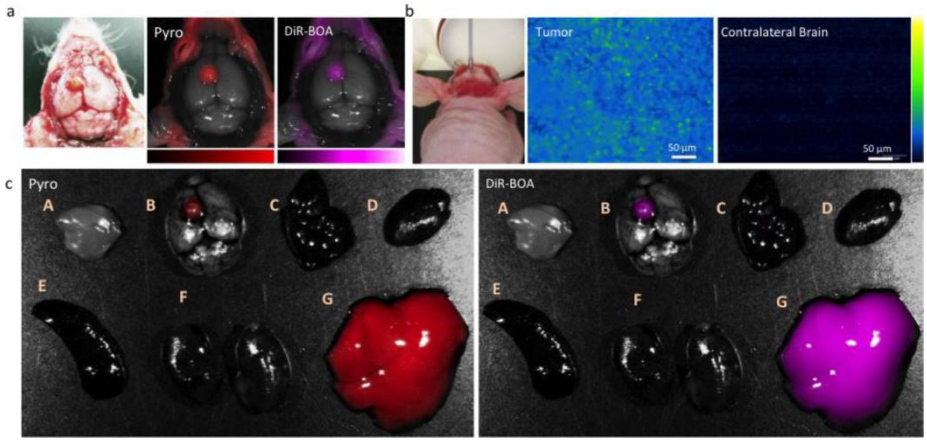

Figure 12. (a) White light photos and corresponding in situ fluorescence images of U87 glioma-bearing mice injected with USPVs at 24 h p.i. Both pyro channel and DiR-BOA channel were acquired. (b) Representative in vivo fluorescence microscopic images obtained with deep red long-pass (Ex: 660 nm, Em 689-900 nm) laser probe. With crania removed, both tumor and contralateral brain were examined. (c) Ex vivo fluorescence imaging of the major organs. Organs in the images are listed as follows, A: Muscle, B: Brain with tumor, C: Lung, D: Heart, E: Spleen, F: Kidneys, G: Liver.

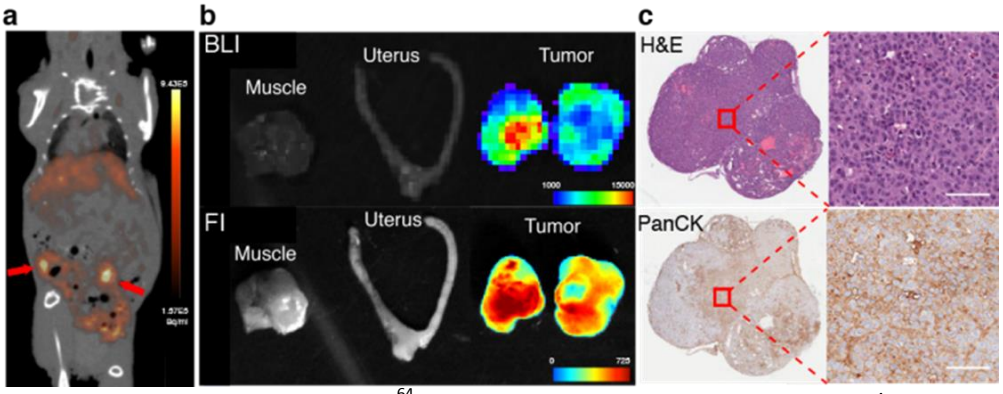

Figure 13. Ovarian cancer metastasis detected by ^{64}Cu-PLP. a. Representative whole-body PET/CT image of mouse with ovarian cancer metastasis after 24 h intravenous injection of ^{64}Cu-PLP (red arrow: tumor). b. *Ex vivo* bioluminescence imaging (BLI) and fluorescence imaging (FI) of metastatic tumors, uterus and muscle. c. The PLP-detected metastases were affirmed by histopathological analysis, showing cancer cell morphology in H&E staining and pancytokeratin (PanCK)-positive (the scale bar in the magnified image: 100 μm).

ADVANCED HEALTHCARE MATERIALS
www.advhealthmat.de

Materials Views
www.MaterialsViews.com

Targeting-Triggered Porphysome Nanostructure Disruption for Activatable Photodynamic Therapy

Cheng S. Jin, Liyang Cui, Fan Wang, Juan Chen, and Gang Zheng**

Photodynamic therapy (PDT) and photothermal therapy (PTT) possess advantages over the conventional therapies with additional treatment selectivity achieved with local laser irradiation. Comparing to PTT that ablates target tissue via thermal necrosis, PDT induces target cell death via singlet oxygen without damaging the underling connective tissue, thus preserving its biological function. Activatable photosensitizers provide an additional level of treatment selectivity via the disease-associated activation mechanism. In this study, folate-conjugated porphysomes are introduced as targeting-triggered activatable nano-sized beacons for PDT. Porphysomes are reported previously as the most stable and efficient delivery system of porphyrin, but their nanostructure converts the singlet oxygen generation mechanism to thermal ablation mechanism. By folate-receptor-mediated endocytosis, folate-porphysomes are internalized into cells rapidly and resulted in efficient disruption of nanostructures, thus switching back on the photodynamic activity of the densely packed porphyrins for effective PDT. In both in vitro and in vivo studies, folate-porphysomes can achieve folate receptor-selective PDT efficacy, which proves the robustness of targeting-triggered PDT activation of porphysome nanostructure for highly selective tumor ablation. The formulation of porphysomes can be modified with other targeting ligands as activatable photosensitizers for personalized treatment in future.

1. Introduction

Photodynamic therapy (PDT) and photothermal therapy (PTT) have emerged as viable clinic approaches that use laser for treatment of diseased tissues during past decades. Both PDT and PTT require the administration of light-absorbing agents, photosensitizers for PDT or thermal enhancers for PTT, combined with local laser irradiation to achieve highly selective treatment,[1,2] but their therapeutic mechanisms are completely different. PTT agents absorb light and dissipate the vibrational energy as heat to destroy targeted tissues within a thermal ablation zone including all connective tissues through a necrosis pathway.[3] Whereas PDT generates singlet oxygen as the predominant cytotoxic agent to damage the region restricted to photosensitizer accumulation, given singlet oxygen's extremely short life time and subsequent short diffusion distance (10–300 nm according to different estimates).[2,4] In many cases, singlet oxygen initiates acute cellular responses leading to the targeted cell death via apoptosis without damaging underlining connective tissues. Therefore, as organ sparing treatment modality, PDT has unique advantages over PTT where preserving the biological function of treated tissues is critical to patients' quality of life, such as esophageal cancer,[5] spinal metastases,[6] etc. Activatable PDT is a relatively new PDT concept introduced to provide an additional level of treatment selectivity over the targeted photosensitizers delivery and precision light delivery.[7,8] Upon laser irradiation, activatable photosensitizers are photodynamic inactive in normal tissue environment as their singlet oxygen generation is silenced, but are turned to be photodynamic active in the diseased area through a variety of activation mechanisms, such as the enzymetic-activation,[9] nucleic acid-activation,[10] and environmental activation (e.g., by pH and hydrophobicity).[11] Therefore, the activatable photosensitizers can achieve a very high level of treatment selectivity by destroying only the targeted cancer cells, while leaving non-targeted (normal) cells unharmed. In this context, several biocompatible nanoparticles-based activatable photosensitizers have been developed for improving their stability, delivery efficiency, and preferential accumulation at target-tissue, such as polymers loaded with porphyrins,[12] but most of them are low of photosensitizers packing density. Recently, we introduced porphysome

C. S. Jin, L. Cui, Dr. J. Chen, Prof. G. Zheng
Ontario Cancer Institute and Techna Institute
University Health Network
101 College Street, Toronto, Ontario M5G 1L7, Canada
E-mail: juan.chen@uhnresearch.ca;
gang.zheng@uhnres.utoronto.ca
C. S. Jin, Prof. G. Zheng
Department of Pharmaceutical Sciences
Leslie Dan Faculty of Pharmacy
University of Toronto
101 College Street, Toronto
Ontario M5G 1L7, Canada
C. S. Jin, Prof. G. Zheng
Institute of Biomaterials and Biomedical Engineering
University of Toronto
101 College Street, Toronto, Ontario M5G 1L7, Canada
L. Cui, Prof. G. Zheng
Department of Medical Biophysics
University of Toronto
101 College Street, Toronto, Ontario M5G 1L7, Canada
L. Cui, Prof. F. Wang
Medical Isotopes Research Center
Peking University
38 Xueyuan Road, Beijing, 10010, China

DOI: 10.1002/adhm.201300651

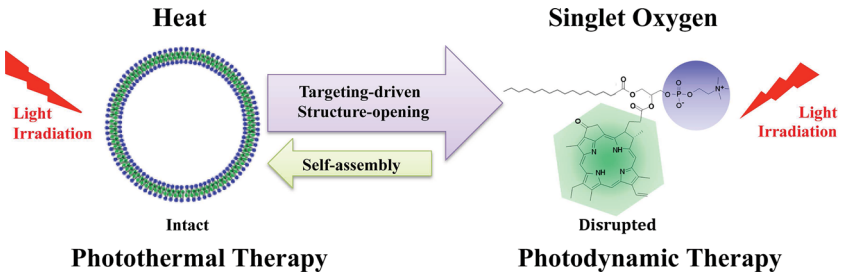

Scheme 1. Schematic illustration of targeting-triggered photodynamic activation of porphysome.

nanostructure that is a liposome-mimicking nanoparticle self-assembled from porphyrin-phospholipid conjugates with high photosensitizers packing density (>80 000/particle), resulting in the nanostructure-induced "super"-absorption and "super"-quenching of photoactivity (fluorescence and singlet oxygen production).[13] We have demonstrated previously that porphysome nanostructure converts the singlet oxygen generating mechanism of porphyrin molecules to a completely thermal mechanism, resulting efficient PTT enhancement.[14] Here, we reported an opposite approach as illustrated in **Scheme 1**, where a targeting-triggered activation mechanism was developed to turn the "super" quenched photosensitizers in intact porphysomes to its photodynamic active stage upon porphysome disruption inside cancer cells, thus providing a new way to design activatable nano-sized beacons for disease-specific PDT. In addition, the densely packed porphyrins in porphysome bilayer provide an unprecedented high payload delivery of photosensitizers to maximize PDT efficacy.

2. Results

2.1. Synthesis and Characterization of Folate-Porphysome

Folic acid is essential for rapid cell division and growth,[16] and binds folate receptor (FR) with high affinity ($K_d \approx 10^{-10}$ M).[17] FR has been found to be overexpressed on various cancer cells, such as ovary, breast, colon, lung, nose, prostate, and brain cancer, and activated macrophages,[18,19] but have limited expression on normal cells.[20] Therefore, FR is widely used as disease targeting biomarker and folate-conjugation has been applied to achieve active FR-targeting delivery of a broad range of theranostics and nanoparticles.[17,19–21] To demonstrate the targeting-triggered activation of porphysome for effective PDT, we synthesized a model FR-targeting porphysome (folate-porphysome) by including 1 mol% of folate-PEG_{2000}-lipid (folate-lipid) in the porphysome formulation and compared its structure, photoactivities (fluorescence and singlet oxygen generation) and structure stability with that of the non-targeting porphysome (the previously reported regular porphysome).[13] Like non-targeting porphysome, the folate-porphysome is spherical vesicle with size around 130 nm in diameter. (Figure S1, Supporting Information), and produces "super"-fluorescence quenching (over 99% quenching efficiency) when it is intact (**Figure 1**a1,b1). The singlet oxygen production of the intact and the nanostructure-disrupted folate-porphysome were further examined and compared with that of non-targeting porphysome under PDT laser (671 nm) irradiation at a wide range of light doses (0.5–10 J cm^{-2}). As shown in Figure 1a2,b2, both folate porphysome and non-targeting porphysome displayed nanostructure-induced "super"-quenching of singlet oxygen generation (over 90% of quenching efficiency) when compared with their corresponding nanostructure-disrupted samples. In addition, both non-targeting porphysome and folate porphysome structures are highly stable either in buffer stock or in serum, evidenced by their fluorescence quenching remained after 24 h incubation in PBS buffer stock and 50% FBS at 37 °C (Figure S2, Supporting Information). Taking together, these data demonstrated that the addition of folate-lipid in the particles formulation does not affect the nanostructure and photoproperties of porphysome.

2.2. Cellular Uptake of Folate-Porphysome and In Vitro Fluorescence Activation

To validate the targeting specificity of folate-porphysome, the cellular uptakes of folate-porphysome and non-targeting porphysome were examined in FR^+ (KB) and FR^- (HT1080) cells by measuring the unquenched porphyrin fluorescence signal in cell lysis buffer. The relative intracellular uptakes were normalized to the uptake of non-targeting porphysome in KB cells. As shown in **Figure 2**a, compared to non-targeting porphysome that displayed similar low uptake in both cell lines, folate-porphysome showed significantly enhanced (58.7-fold) uptake in FR positive KB cells after 3 h incubation (Figure 2a), but much less enhanced (8.2-fold increase) uptake in FR low expression HT1080 cells. When increasing the incubation time from 3 to 24 h, the uptake of non-targeting porphysome in both KB and HT1080 was negligibly increased (<0.5 fold), while the uptake of folate-porphysome was dramatically increased (172 fold) in KB cells (FR^+) and slightly increased (24 fold) in HT1080 cells (FR^-) (Figure 2b). In addition, the enhanced uptake of folate-porphysome in KB cells either for 3 or 24 h incubation can be completely inhibited by free folic acid. These data demonstrated the specific FR-targeting enhanced intracellular uptake of folate-porphysome.

The FR-targeting-triggered fluorescence activation was further assessed by confocal imaging. Although folate-porphysome showed efficient uptake in KB cells after 3 h incubation (Figure 2a), confocal imaging showed very weak fluorescence signal right after 3 h incubation, which indicated the folate-porphysomes being intact nanostructure after initial internalization (Figure 2c). Waiting for additional 21 h in regular cell culture condition, these cells showed much stronger porphyrin fluorescence (Figure 2d), suggesting that the disruption of folate porphysome nanostructure in cells is a time-consuming process, which resulted in gradual unquenching of porphyrin photoproperties. The specific FR-mediated fluorescence activation of folate-porphysomes was further validated by the effective inhibition using free folic acid (Figure 2d). In contrast, the

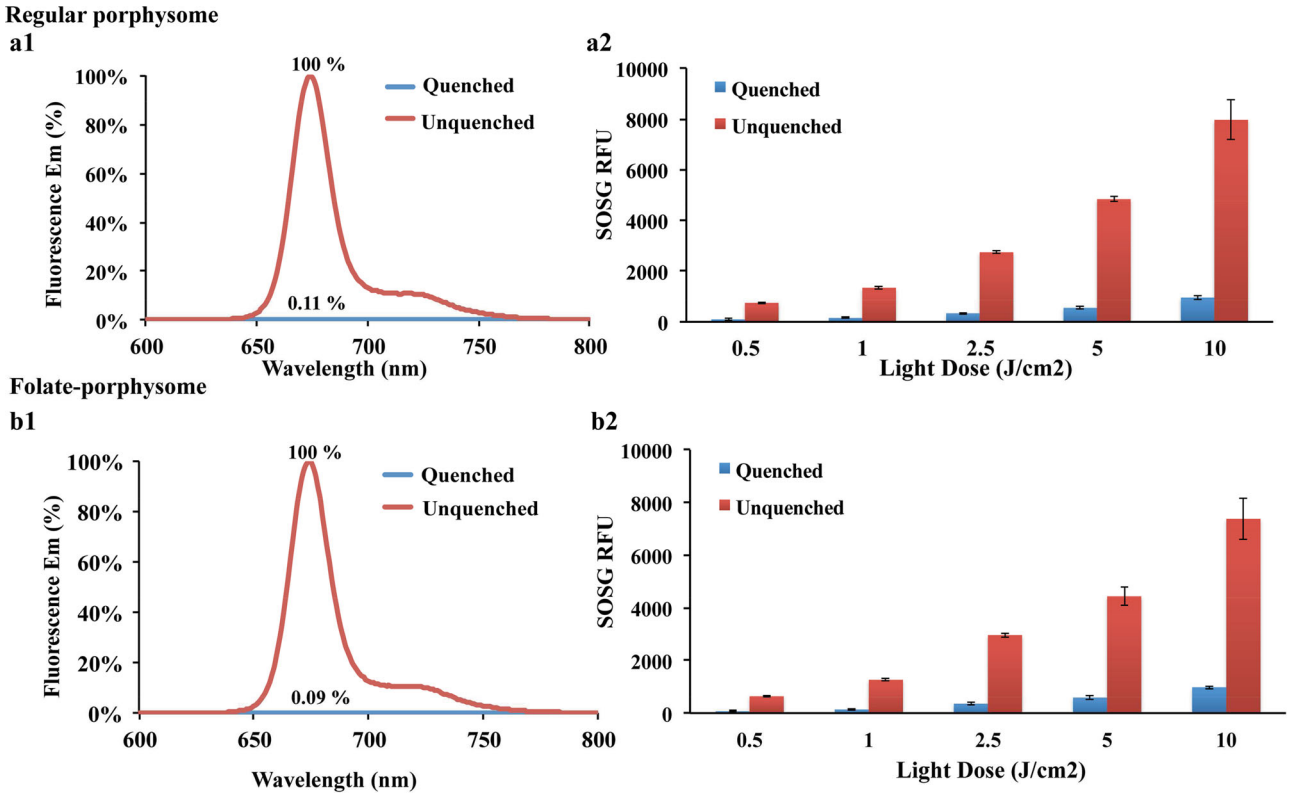

Figure 1. The characterization of fluorescence and singlet oxygen generation of porphysomes. a1) Fluorescence emission of intact (quenched) versus disrupted non-targeting porphysomes (unquenched). a2) Singlet oxygen generation reported by SOSG fluorescence intensity upon laser irradiation (671 nm, 50 mW cm^{-2}) for intact versus disrupted porphysomes at light dose from 0.5 to 10 J cm^{-2}. b1) Fluorescence emission of intact (quenched) versus disrupted folate-porphysomes (unquenched). b2) Singlet oxygen generation reported by SOSG fluorescence intensity upon laser irradiation (671 nm, 50 mW cm^{-2}) for intact versus disrupted folate-porphysomes at light dose from 0.5 to 10 J cm^{-2}.

control non-targeting porphysome did not show any fluorescence activation in cells at either 3 h right after incubation or 21 h later.

2.3. Validation of Targeting-Triggered PDT Activation of Folate-Porphysome in FR^+ Cancer Cells

To verify in vitro PDT activation of folate-porphysome after targeting-enhanced intracellular uptake, cell viability (MTT assay) was measured on the KB cells (FR+) with and without laser treatment. The cells treated with non-targeting porphysome were used as a control and the cell viability of each group was normalized to that of the untreated cells. As shown in **Figure 3**, neither non-targeting porphysome nor folate-porphysome had noticeable dark toxicity to cells at the porphyrin concentration of 5×10^{-6} M. Upon PDT laser treatment (671 nm, 10 J cm^{-2}), non-targeting porphysome induced minor photocytotoxicity (96.4 ± 8.5% of cell viability) while folate-porphysome decreased significantly the cell viability to 38.5 ± 4.3%. Together with effective inhibition of the photocytotoxicity of folate-porphysome by extra free folic acid (93.1 ± 7.4% of cell viability), these results suggested that the targeting-enhanced intracellular uptake and photoactivation of folate-porphysome ultimately resulted in significant improvement on PDT therapeutic outcomes.

2.4. In Vivo Fluorescence Activation of Folate-Porphysome on KB-Tumor-Bearing Mice

Both fluorescence and singlet oxygen generation of porphyrin molecules are highly quenched in intact porphysomes, but are significantly activated when the nanostructure is disrupted (Figure 1), Therefore, fluorescence activation could serve as a useful indicator for assessment of the nanostructural disruption and singlet oxygen ($^1O_2$) activation. The in vivo fluorescence activation of the porphysomes was examined on KB-tumor-bearing mice with intravenous administration of non-targeting or folate porphysomes. As shown in **Figure 4**a, mice injected with folate-porphysome started to show fluorescence contrast in tumor over surrounding normal tissue as early as 6 h post-injection, while non-targeting porphysome did not display obvious fluorescence contrast in tumor area at that time point. After 24 h administration, tumor fluorescence increased significantly in folate-porphysome group, but was much weaker in non-targeting porphysome group. To investigate whether the folate porphysomes giving enhanced fluorescence in tumor

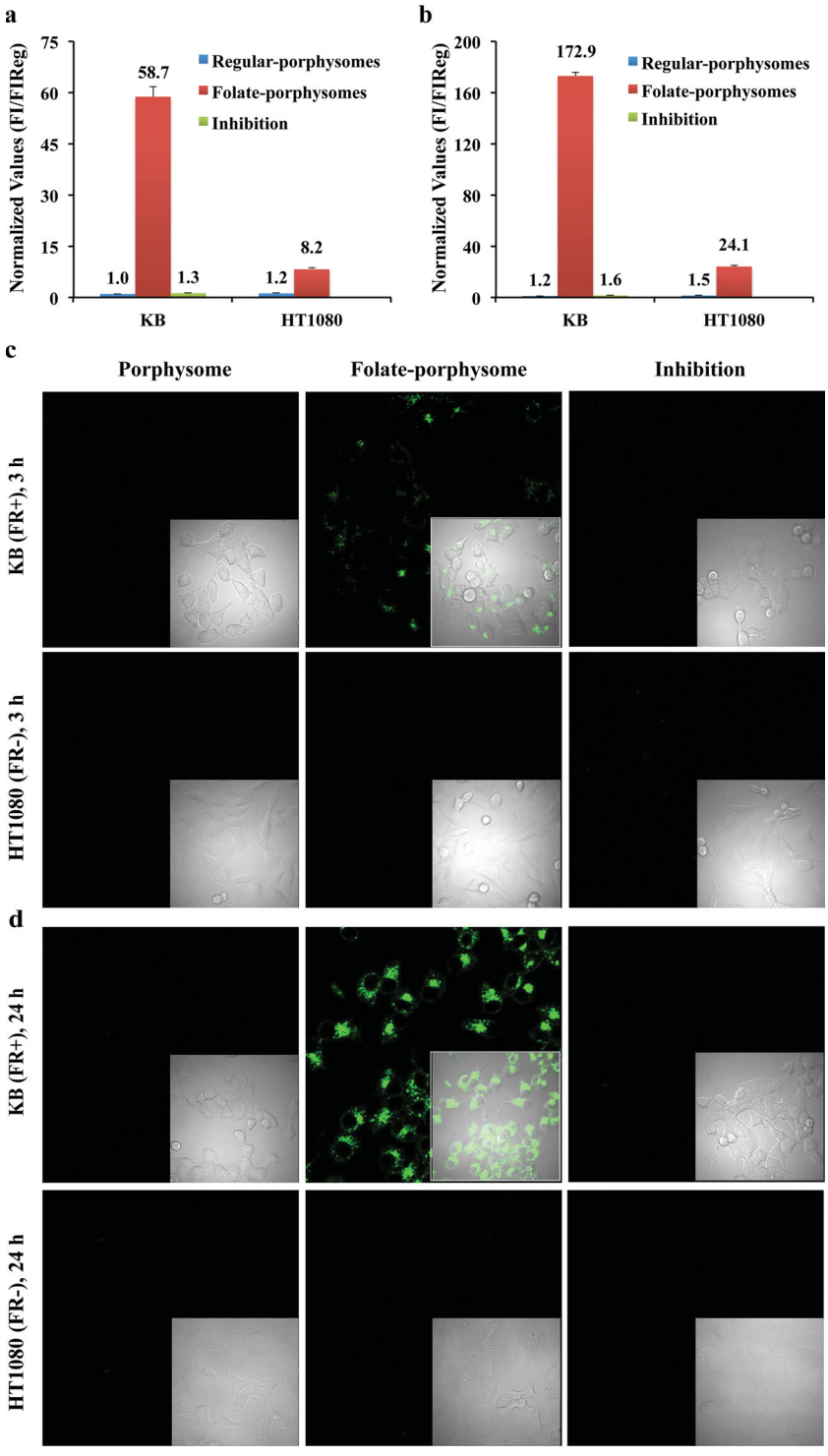

Figure 2. Quantitative cellular uptake and fluorescence activation of non-targeting porphysome, folate-porphysome, and folate-porphysome with folic acid inhibition in KB cells (FR^+) and HT1080 cells (FR^-). Intracellular uptakes were quantified by measuring porphyrin fluorescence signal in cell lysis buffer at a) 3 h and b) 24 h incubation of porphysome samples. The relative intracellular uptakes were normalized to the uptake of non-targeting porphysome in KB cells. The confocal fluorescence imaging of the KB and HT1080 cells (c) right after 3 h incubation and (d) 21 h post 3 h incubation with non-targeting porphysomes, folate porphysomes, and folate-porphysomes with free folic acid (porphyrin concentration: 5×10^{-6} M).

compared to non-targeting porphysomes is due to a higher tumor accumulation, we examined the tumor accumulation of two porphysomes by using radioisotope ^{64}Cu labeling procedure.[15] Surprisingly, we observed that the tumor accumulation of folate-porphysome was even worse than that of non-targeting porphysome at either 6 h (4.4 vs 8.1 %ID/g) or 24 h (3.1 vs 7.6 %ID/g) (Figure 4b) post-administration, indicating the enhanced fluorescence in tumor of folate-porphysome group was attributed by quicker fluorescence activation. Altogether, these data suggest that FR targeting significantly accelerated the in vivo fluorescence activation of porphysomes in tumor.

2.5. In Vivo PDT Efficacy of Folate-Porphysomes

Although non-targeting porphysome has been demonstrated as an efficient PTT agent upon high power laser irradiation (671 nm, 750 mW cm^{-2}),[13,22] the in vivo PDT treatment was performed at much lower laser setting (671 nm, 150 mW cm^{-2}, 100 J cm^{-2}). The tumor temperature during the PDT treatment was monitored in real time by a thermal camera to ensure that the experimental laser treatment did not cause PTT effect. As shown in **Figure 5**a, no significant temperature increase (tumor temperature remained around 35 °C constantly) was observed for all laser treatment groups during the 10 min treatment, indicating that no PTT contribution was involved in the treatment. The PDT treatment efficacy was firstly evaluated by monitoring tumor growth rate. The tumor-bearing mice without any treatment served as blank control. As shown in the Figure 5b, the tumors received either the laser treatment or folate-porphysomes injection alone remained the same tumor growth trend as that of blank controls, indicating that neither PDT laser nor folate-porphysomes induced any therapeutic effect. Folate-porphysome plus PDT laser completely inhibited the tumor growth, while non-targeting porphysomes plus PDT laser negligibly decrease the tumor growth, which demonstrated the folate-targeting-triggered photodynamic activation of porphysomes in tumor.

The mice survival study was further conducted after treatment (Figure 5c). For the groups (n = 5/group) of blank control, PDT laser alone, and folate-porphysomes

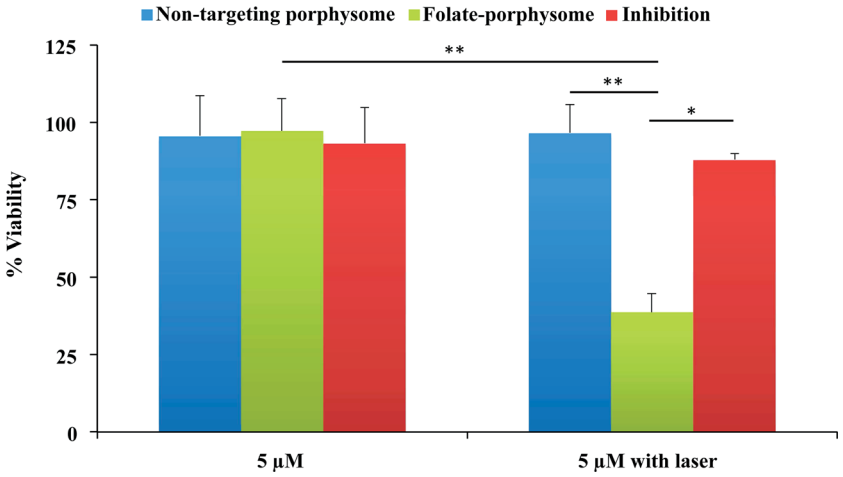

Figure 3. The targeting-triggered PDT activation of porphysome was investigated by measuring the cell viability with and without laser treatment using MTT assay. PDT treatment method: 671 nm laser at 10 J cm^{-2}. Cell viability was normalized to that of the untreated cells.

alone, tumors appeared unaffected and grow continuingly (Figure 5d) to reach the end point completely at day 12, 10, and 12, respectively (Figure 5c). For the mice received non-targeting porphysome plus laser, no obvious tumor ablation was observed after treatment (Figure 5d) and the tumors started to reach the end point at day 4 (80%) post-PDT treatment and ended completely at day 13 post-PDT (Figure 5c). For the animals treated with folate-porphysomes plus laser, the treated tumor tissue became swollen at day 2 post PDT, displayed dark brown ablation from day 3 post-PDT (Figure 5d), and the tissues slowly recovered in the following 2 weeks with 80% survival rate (Figure 5c). To further investigate the PDT response on the cellular level, another set of treatment groups was scarified at 24 h post-PDT and the tumors and some normal organs, including tumor surrounding muscles, livers, kidneys, and spleens, were harvested for H&E histology analysis. As expected, only the tumor from the mice received folate-porphysome plus laser showed clear cellular damage, while the tumors from other groups did not (**Figure 6**), confirming the specific folate-porphysome-enabled PDT efficacy. In addition, no obvious cellular damage and morphology change were observed in the collected normal organs for all treatment groups when compared to that of non-treated blank control, indicating that the folate porphysome-enabled PDT is a safe treatment procedure.

3. Discussion

Activatable photosensitizer has drawn tremendous attention as it combines the concept of local treatment and personalized therapy. The well-designed activatable PDT agents display minimal phototoxicity in their inactive states, and become photodynamic active only in the targeted tissue to provide an additional level of PDT selectivity for preservation of the critical connective tissues, thus improving the PDT therapeutic index.[7]

Both endogenous and exogenous porphyrins have been studied as diagnostic and therapeutic agents, with wide acceptation for clinic trial of PDT and PTT.[7] Porphysomes constructed from extremely high density of porphyrin–phospholipid (>80 000/particle) provide a nanostructure-induced "super"-absorption and "super"-quenching of porphyrins' photoactivity, resulting in unique nanostructure-dependent photo-therapeutic function. The intact porphysome nanostructure converts the singlet oxygen generating mechanism of porphyrin molecules to a completely thermal mechanism, resulting in efficient PTT enhancement.[13,22] Here, we demonstrated a targeting-triggered activation mechanism to "turn back on" the suppressed singlet oxygen generation of the intact porphysomes upon porphysome disruption inside the targeted cells, thus providing an ideal "activatable photodynamic nanobeacon." First, the nanostructure-induced "super quenching" minimizes the phototoxicity of the intact porphysome during its systemic delivery. Secondly, the densely packed porphyrins in the porphysome bilayer provide an unprecedented high payload delivery of photosensitizers to maximize PDT efficacy. Finally, the targeting ligand not only improves the delivery selectivity, but also accelerates the particles' internalization and disruption in cells, thus "turning on" the photodynamic activity for effective PDT.

Using folate-porphysome as a model, we demonstrated that the folate-receptor-mediated endocytosis enables a quick active accumulation of the particles, which consequently triggers the unquenching of the porphyrin's photoproperties in cells. The results (Figure 2) showed that even though the targeting-mediated uptake of particles is very fast, the fluorescence activation in cells is a time-consuming process and the maximum fluorescence intensity was achieved at 24 h post-incubation. Accordingly, in vitro PDT was performed at 24 h post-incubation and a selective photocytotoxicity was achieved in FR+ cancer cells with great efficiency.

The receptor-mediated endocytosis activation strategy is ascertained in the in vivo studies. It is somewhat surprising that the accumulation of folate-porphysome in tumor was relatively lower than that of non-targeting porphysome. For nanoparticles with size around 100 nm, enhanced permeability and retention (EPR) effect usually dominates their tumor accumulation. A prolonged circulation time would facilitate the filtration of nanoparticles from the blood circulation directly into the tissues and enhance the retention of the particles in the diseased area. By investigating the pharmacokinetics of these particles, we found that folate porphysome has much shorter blood circulation half life (<4 h) than non-targeting porphysome (10 h) (Figure S3, Supporting Information), which could explain the lower accumulation of folate porphysome in tumor. Interestingly, the less uptake of folate-porphysome in tumor results in more efficient activation in tumor when compared to non-targeting porphysome. The explanation could be that folate porphysome was actively delivered into tumor cells to undergo efficient photodynamic activation and achieve efficient therapeutic outcomes. Whereas non-targeting porphysome showed a

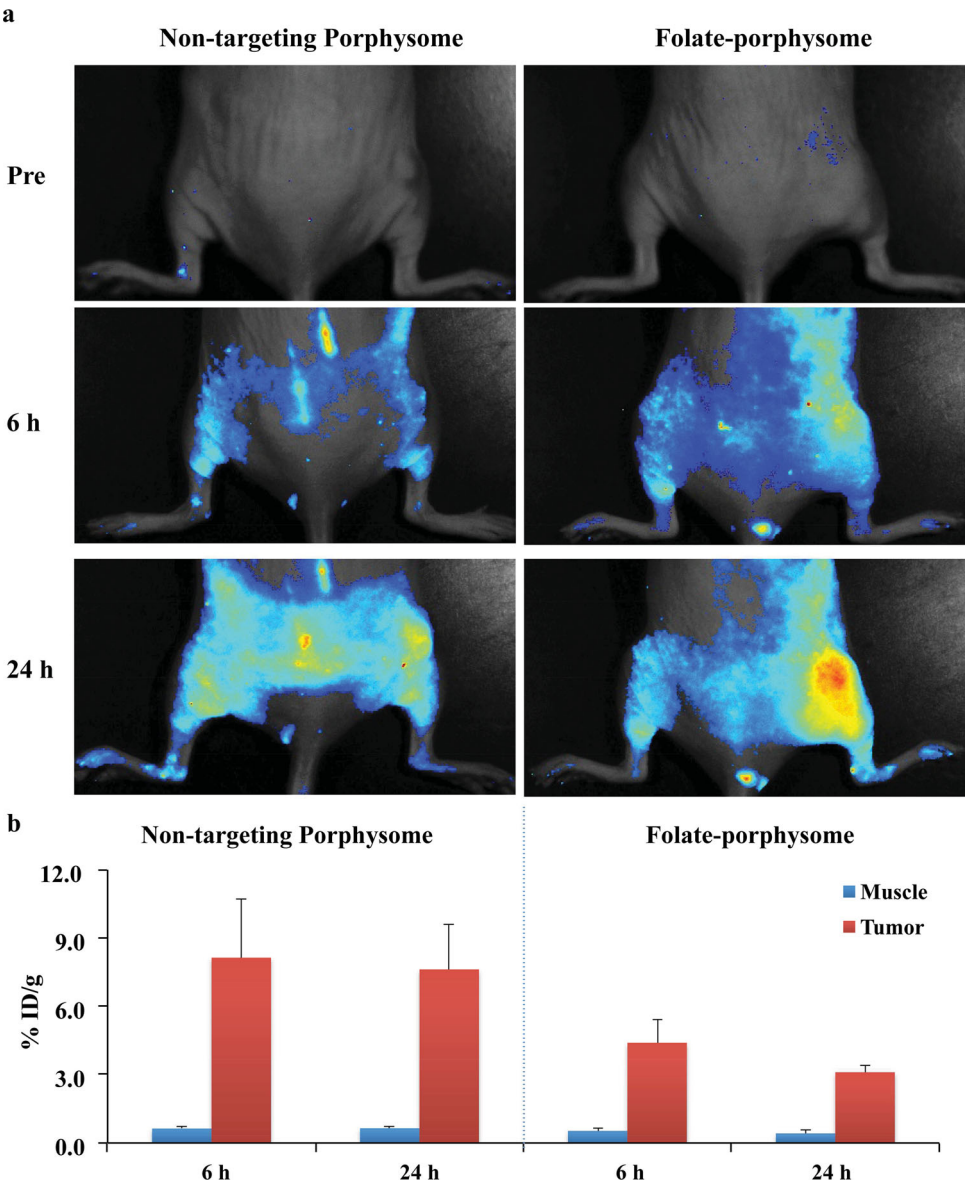

Figure 4. In vivo fluorescence activation and quantification of uptake in tumor versus muscle in KB-tumor-bearing mice. a) Fluorescence image of animals at pre-injection, 6 and 24 h-post i.v. injection of non-targeting and folate-porphysomes with a dose of 10 mg kg^{-1}. b) Accumulation of ^{64}Cu-labeled porphysomes in muscle and tumor at 6 h and 24 h post-injection were quantified by γ–counting approach, plotted as% injected dose/gram (%ID/g). ($n = 4$)

higher uptake in tumor, but mostly accumulated in the interstitial space through EPR effect, thus PDT remains inactive upon treatment. The contradiction of accumulation and treatment efficacy for non-targeting porphysome and folate-porphysome strongly supports the targeting-triggered PDT activation of porphysome. Folate-porphysome used in this study contained relatively higher percentage of folate-PEG2000-DSPE (1 mol%) when compared to that typically used in FR-targeted liposomes (0.3–0.5 mol%), where folate modification did not significantly affect liposome half life.[23] This higher folate ratio may alter the surface property of the porphysomes and consequently affect their in vivo pharmacokinetics and biodistribution. The delivery efficiency could be easily improved by optimizing the ratio of folate-ligand.[24] Given folate-liposome with desirable pharmacokinetics has been well-developed[24,25] and porphysome is a liposome-mimicking nanoparticle, it will not be difficult to optimize folate-porphysome formulation to prolong the circulation time while preserving the receptor-mediated activation capacity.

The targeting-triggered porphysome nanostructure disruption provides a highly versatile platform for activatable PDT. Apart from folate-targeting, it can be easily adopted for targeting other disease-specific biomarkers, such as EGF receptor. It can also be functionalized with various targeting moieties, such as antibody, antibody fragments, peptides, aptamers,

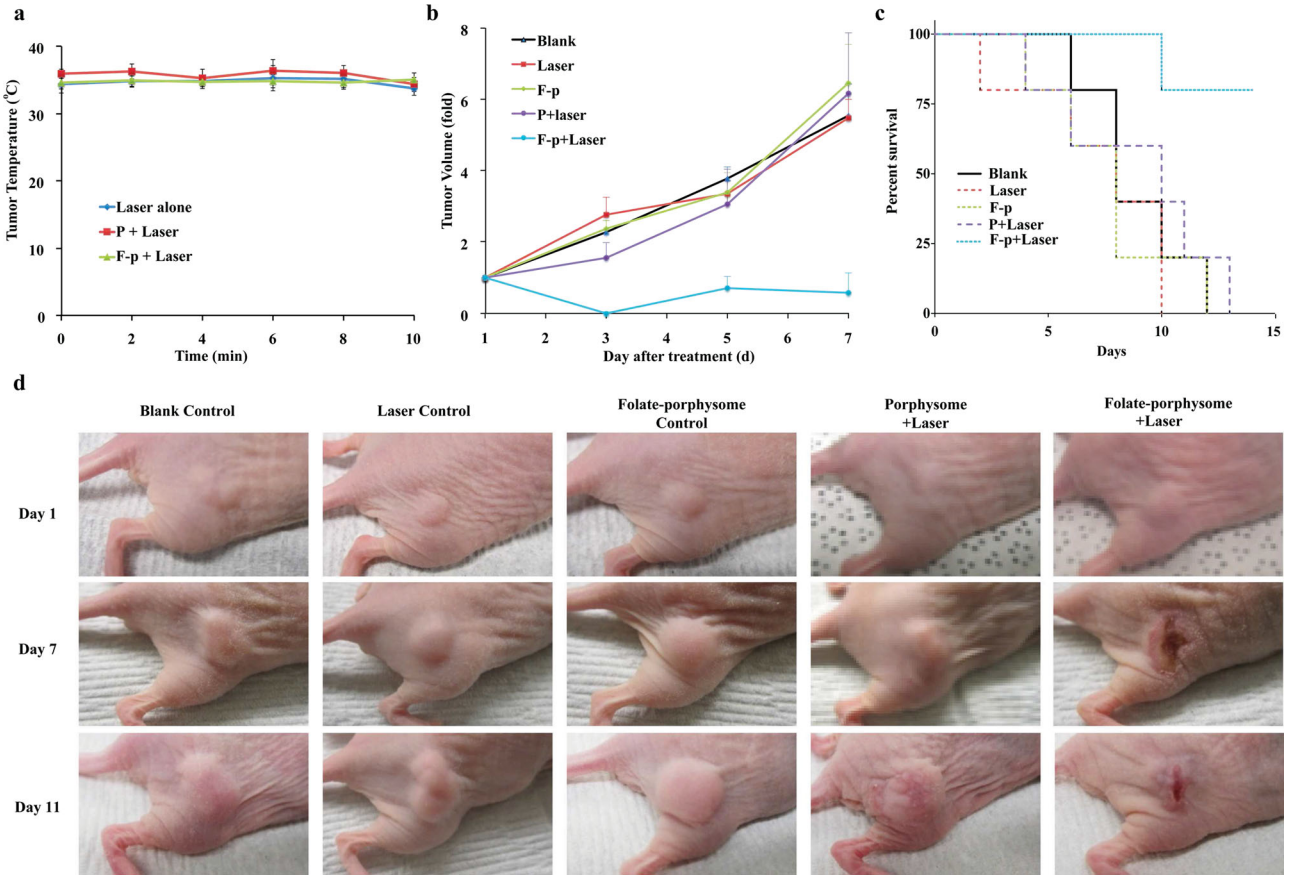

Figure 5. In vivo PDT treatment response in KB-tumor-bearing mice. Mice were injected with non-targeting and folate-porphysomes at a dose of 10 mg kg^{-1}. a) Real-time monitoring of tumor temperature during 10 min laser irradiation. b) Tumor growth curve after treatment for each group ($n = 5$). c) Survival curve of animals after treatment for each group ($n = 5$). Folate porphysome(F-p), non-targeting-porphysome plus laser (P+laser), and folate-porphysome plus laser (F-p+laser). d) Representative mice tumor images at day 1, day 7, and day 14 post PDT treatment.

glycoproteins (e.g., transferrin) and small molecule,[26] to achieve personalized treatment planning.

The liposomal-like nanostructure and unique photonic and physiochemical properties make porphysome a good candidate of all-in-one multifunctional nanoconstruct.[27] The liposome-like bilayer structure enables porphysomes to carry a variety of therapeutic and imaging agents.[13] In addition to the fluorescence imaging, the inherent advantages of porphysome on capable of direct chelating radioisotopes, such as ^{64}Cu, enables noninvasive quantitative biodistribution study, and faithful tracking of the fate of nanoparticle-based drug delivery.[15,28] The multifunctionality of porphysomes together with the smart PDT activation property makes porphysomes suitable for multimodal imaging and therapeutic application for future personalized cancer treatment.

4. Conclusions

Folate-porphysomes were constructed by incorporating a small molar percentage of folate conjugate lipid in porphysome formulation, which enabled FR-mediated cell uptake of nanoparticles and resulted in rapid nanostructure disruption in cells to ultimately trigger the unquenching of porphyrin fluorescence as well as singlet oxygen generation. Upon laser irradiation, folate-porphysomes achieved folate receptor-selective PDT efficacy. After systematically administrated to FR-positive tumor-bearing mice, folate-porphysomes were capable to reduce the tumor burden by PDT and ameliorated the overall survival. Therefore, FR receptor targeting-triggered nanostructure disruption provided an activation method for switch back on the suppressed singlet oxygen generation of the intact porphysomes inside the targeted cells, thus enhancing PDT efficiency and specificity. Furthermore, targeting-porphysome formulation can be modified with a variety of targeting moieties to achieve disease–specific activatable PDT for future personalized cancer treatment.

5. Experimental Section

5.1. Porphysomes Synthesis

Porphysomes with or without folate-targeting ligands were formed using a protocol reported previously.[13] The lipid film for non-targeting

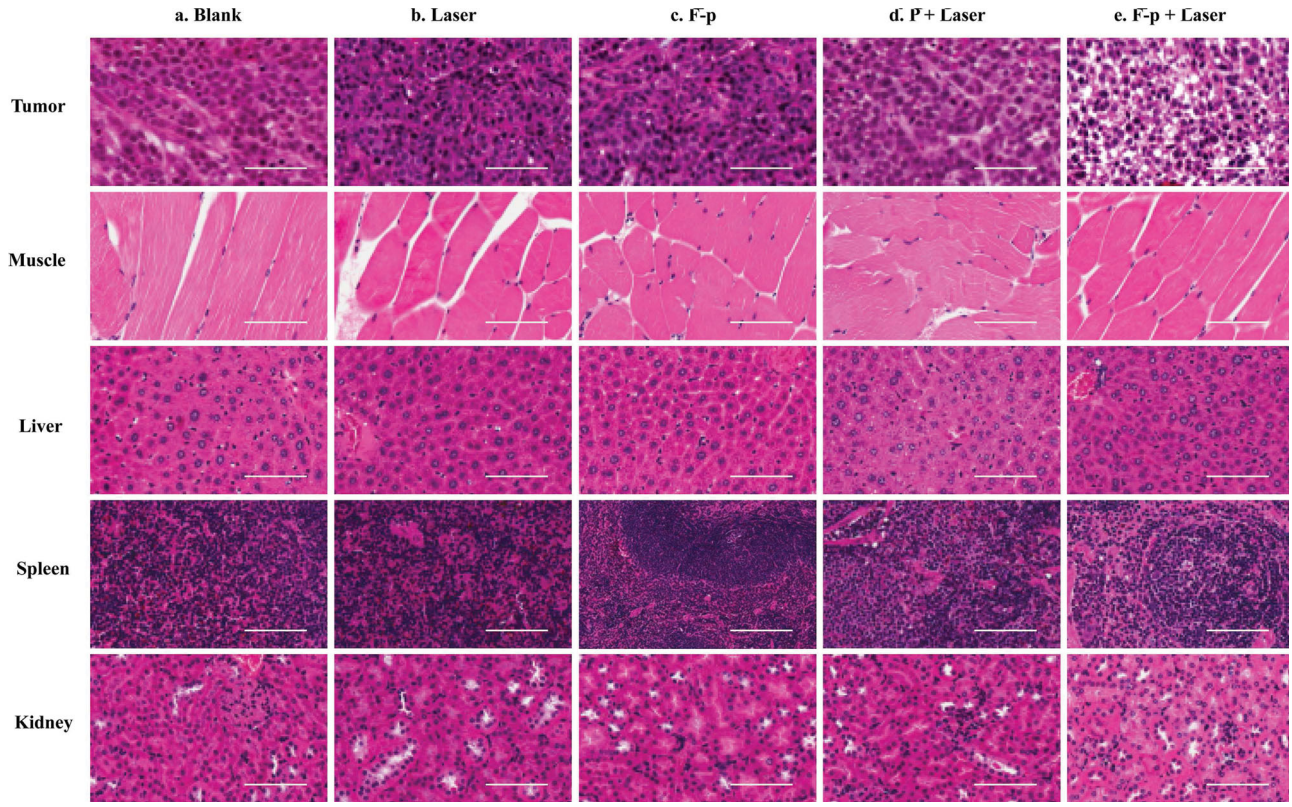

Figure 6. H&E staining of tumor, surrounding muscle, liver, spleen, and kidney tissue slices for different groups: blank control, laser alone, folate porphysome(F-p), non-targeting-porphysome plus laser (P+laser), and folate-porphysome plus laser (F-p+laser), at 24 h post PDT treatment.

porphysome (regular porphysome) consists of 55 mol% of porphyrin-lipid (pyropheophorbide-lipid), 40 mol% of cholesterol (Avanti Polar Lipids), and 5 mol% of distearoyl-sn-glycero-3-phosphoethanolamine-N-methoxy(polyetheneglycol) (PEG2000-DSPE; Avanti Polar Lipids). For folate-porphysome, 4 mol% PEG2000-DSPE was supplemented with 1 mol% 1,2-distearoyl-sn-glycero-3-phosphoethanolamine-N-folate(polyethylene glycol) (Folate-PEG2000-DSPE; Avanti Polar Lipids). Lipid films were dried under a gentle stream of nitrogen gas and the residue solvent was removed via 1 h vacuuming. The dried lipids were kept at −20 °C under argon prior to use. To prepare the particles, each lipid film was rehydrated with 1.0 mL PBS buffer (150×10^{-3} M, pH 7.5) and extruded through a polycarbonate membrane (pore size = 100 nm) for 10 times. Final size of the particles was measured by dynamic light scattering (ZS90 Nanosizer, Malvern Instruments) and the porphyrin concentration was determined by UV–Vis spectrometer (Varian Inc., Palo Alto, CA). Both non-targeting porphysomes and folate-porphysomes were freshly prepared and kept sterile prior to use.

5.2. Fluorescence Quenching Efficiency and Singlet Oxygen Generation

The fluorescence of intact porphysomes and disrupted porphysomes was measured to calculate the fluorescence quenching efficiency. Non-targeting porphysomes and folate-porphysomes were diluted in either PBS as intact/quenched samples or 1% Triton X-100 as disrupted/unquenched samples at the concentration of 1×10^{-6} M of porphyrin-lipid amount. The samples were then subjected to Spectrofluorometer for fluorescence measurement (Excitation: 420 nm, Emission: 600–800 nm, slit width: 2 nm). The fluorescence emission (%) for different porphysomes was presented as the fluorescence signal at 675 nm normalized to their corresponding disrupted samples. Singlet oxygen generation of non-targeting porphysomes and folate-porphysomes (both intact and disrupted porphysomes) was measured.

The singlet oxygen sensor green (SOSG) reagent (Molecular Proves, Inc.) was employed for the detection of singlet oxygen in porphysome and folate-porphysome solution following manufacturer protocols. A freshly prepared SOSG solution in methanol (5×10^{-3} M) was mixed with porphysome or folate-porphysome (1×10^{-6} M porphyrin amount), intact in PBS or disrupted with 0.5% Triton X-100, to a final SOSG concentration of 6×10^{-6} M. Samples were treated with an array of light-emitting diodes at 671 nm with a fluence rate of 50 mW cm^{-2} at the light dose from 0.5 to 10 J cm^{-2}, and SOSG fluorescence was measured by exciting at 488 nm and collecting at 525 nm. There was no porphyrin fluorescence contribution within this emission window.

5.3. Confocal Microscopy and Quantitative Cellular Uptake Study

To investigate the folate-receptor-mediated cell internalization and targeting-triggered activation of fluorescence, confocal imaging was conducted to monitor the porphyrin fluorescence after cell incubation. KB cells (FR+) were cultured in RPMI 1640 media (Lonza) with 10% FBS and HT1080 (FR-) were cultured in EMEM media (ATCC) with 10% FBS. For confocal study, 2×10^4 cells/well were seeded in eight-well chamber slides 24 h prior to incubation. Cells were incubated with non-targeting porphysomes, folate-porphysomes, and folate-porphysomes with free folic acid (1×10^{-3} M, as inhibitors) at porphyrin concentration of 5×10^{-6} M for 3 h at 37 °C. Cells were then rinsed by PBS for three times

and continued to grow in fresh cell culturing media. Cells were imaged by confocal microscopy (Olympus FluoView 1000) right after the cell incubation and 24 h later to monitor the unquenching profile of the fluorescence. For quantitative cellular uptake study, KB and HT1080 cells were seeded in a six-well plate (10^6 cells per well) 24 h prior to porphysomes' incubation. Cells were incubated with non-targeting porphysome, folate-porphysome, and folate-porphysome plus folic acid (1×10^{-3} M, as inhibitors) at the porphyrin concentration of 5×10^{-6} M for 3 h at 37 °C, and then rinsed three times with PBS. 100 µL lysis buffer was added to each well and the plate was placed on ice for 30 min. The cytosol content of each treatment group was harvested and centrifuged at 12 000 rpm for 10 min, and the fluorescence of porphyrin in the supernatant was measured by Spectrofluorometer (HORIBA Scientific Inc.), to calculate the amount of porphyrin that had been uptaken by cells at each treatment condition.

5.4. In Vitro PDT and Dark Toxicity

To verify the activatable photocytotoxicity of folate-porphysomes, in vitro PDT treatment and dark toxicity studies were conducted. KB cells (FR+) were seeded (5×10^3 cells per well) in 96-well plates 24 h prior to porphysomes' incubation. Then, cells were incubated with 5×10^{-6} M non-targeting porphysome, folate-porphysome, and folate-porphysome plus free folic acid (1×10^{-3} M, as inhibitors). After 3 h incubation at 37 °C, cells were washed three times with PBS and changed to fresh medium. Waiting for additional 21 h, cells were subjected to PDT treatment by using a 671 nm continuous wavelength laser with light dose of 10 J cm^{-2}. 24 h later, cells were incubated with 0.5 mg mL^{-1} of MTT solution (3-(4,5-dimethylthiazol-2-yl)-2,5-diphenyltetrazolium bromide, Invitrogen) for 2 h. The media were then replaced with 150 µL of 1:1 DMSO/70% isopropanol in 0.1 M HCl, shaken for 30 min and the absorbance at 570 nm was measured to determine the cell viability relative to the untreated control. The cells that were incubated with porphysomes as described above but did not receive laser irradiation were tested for dark toxicity of non-targeting porphysome and folate porphysome.

5.5. Animal Preparation and Tumor Model

All animal experiments were performed in compliance with University Health Network guidelines. The animal studies were conducted on nude mice with KB xenografts. Nu/nu nude female mice were purchased from Harlan Laboratory and kept in the Animal Research Centre of University Health Network. KB cells were cultured in RPMI-1640 media with 10% FBS. 2×10^6 KB cells were inoculated subcutaneously in the nude mice and the experiments were conducted approximately 10 days post-inoculation when the tumors attained a surface diameter of 4–5 mm or with the volume around 30 mm^3.

5.6. Biodistribution and Blood Clearance

When the tumors reached the diameter of 4–5 mm, non-targeting porphysome and folate-porphysome were first chelated with radioisotope ^{64}Cu, following the previously described protocol,[15] and then i.v. injected to animals at the dose of 10 mg kg^{-1} porphyrin amount (n = 4 in each group). At 6 h or 24 h post-injection time points, animals were sacrificed and tumors were harvested. The mass and radioactivity of tumors were measured and calculated for the porphyrin accumulation at each time point as%ID/g.

5.7. In Vivo Fluorescence Imaging

To study the fluorescence-activation of porphysomes upon tumor accumulation in vivo, the fluorescence of animals was monitored at series of time points after the systematic administration of non-targeting porphysomes and folate-porphysomes. When tumor reached 4 to 5 mm diameter or 30 mm^3, animals were fed with low-fluorescence diet (Harlan Tekland, Product No. TD.97184) for 3 d before porphysomes' administration. Non-targeting porphysomes or folate-porphysomes were then injected through tail vein at a dose of 10 mg kg^{-1}, calculated on the porphyrin content. Animals were imaged using a Maestro imaging system (CRI, USA) using a 575–605 nm excitation filter and an 645 nm long-pass emission filter at three time points: before the injection, 6 and 24 h post-injection.

5.8. Photodynamic Therapy

The PDT efficacy of non-targeting porphysome and folate-porphysome was investigated using KB-tumor-bearing mice. Five groups were included for comparison: blank control group without any treatment; PDT laser treatment alone; folate-porphysomes injection alone; non-targeting porphysomes plus PDT laser treatment; and folate-porphysomes plus PDT laser treatment. When tumors reached 4 to 5 mm diameter or 30 mm^3, porphysomes were i.v. injected to animals at a dose of 10 mg kg^{-1}, calculated on the porphyrin content. At 24 h post-injection, mice were anesthetized with 2% (v/v) isoflurane and tumors were irradiated with a 671 nm laser (DPSS LaserGlow Technologies, Toronto, Canada). The laser intensity was measured as 150 mW cm^{-2} with a spot size of 9 mm diameter, and the total light dose was 100 J cm^{-2}. Temperature changes of tumors for the groups of laser alone, non-targeting porphysomes PDT, folate-porphysome PDT were monitored using an infrared thermal camera (Mikroshot, LUMASENSE Technologies), and were calculated with n = 5 in each treatment group for average and standard deviation.

5.9. Treatment Responses

To evaluate the therapeutic efficacy tumor growth rate and survival study (n = 5), and histology study (n = 3) were conducted. To monitor the tumor growth after treatment, tumor size was measured with a Vernier caliper once every 2 d. The volume was calculated as $V = \pi/6 \times a \times b^2$ with n = 5 in each treatment group for average and standard deviation of tumor volumes. Mice were euthanized at the defined end point when the tumor volume reached 300 mm^3, and survival curve was plotted accordingly. For H&E histology analysis, tumors and surrounding organs (liver, spleen, kidney, and muscle) were harvested and fixed in 10% formaldehyde at 24 h post-treatment for histology studies. Tumors were then sectioned into slices of 8 µm thickness and H&E staining was carried out by standard methods at the Pathology Research Program Laboratory at University Health Network. The sections were viewed and photographed by bright field microscopy at 20×.

5.10. Statistical Analysis

The Student's t-test (two-tailed) was used to determine the statistic significance of the difference when comparing different treatment groups.

Acknowledgement

C.S.J. and L.C. contributed equally to this work. The authors thank Marta Overchuck for the assistance in cell culture and animal experiment. This work was supported by grants from the Canadian Institute of Health Research, the Canadian Space Agency, the Prostate Cancer foundation of Canada, the Natural Sciences and Engineering Research Council of Canada, the Canadian Foundation for Innovation, US Army Grant #

W81XWH-13–1–0442, the MaRS Innovation, Canadian Cancer Society Research Institute, the Princess Margaret Cancer Center Foundation, and the Joey and Toby Tanenbaum/Brazilian Ball Chair in Prostate Cancer Research.

Received: November 22, 2013
Revised: December 16, 2013
Published online: January 27, 2014

[1] P. Rai, S. Mallidi, X. Zheng, R. Rahmanzadeh, Y. Mir, S. Elrington, A. Khurshid, T. Hasan, *Adv. Drug Delivery Rev.* **2010**, *62*, 1094.
[2] T. J. Dougherty, C. J. Gomer, B. W. Henderson, G. Jori, D. Kessel, M. Korbelik, J. Moan, Q. Peng, *J. Natl. Cancer Inst.* **1998**, *90*, 889.
[3] a) G. Jori, J. D. Spikes, *J. Photochem. Photobiol. B* **1990**, *6*, 93; b) S. N. Goldberg, G. S. Gazelle, P. R. Mueller, *AJR Am. J. Roentgenol.* **2000**, *174*, 323.
[4] a) I. J. MacDonald, D. J. Dougherty, *J. Porphyrins Phthalocyanines* **2001**, *105*; b) B. C. Wilson, M. S. Patterson, *Phys. Med. Biol.* **2008**, *53*, R61.
[5] A. Sibille, R. Lambert, J. C. Souquet, G. Sabben, F. Descos, *Gastroenterology* **1995**, *108*, 337.
[6] T. W. Liu, M. K. Akens, J. Chen, L. Wise-Milestone, B. C. Wilson, G. Zheng, *Bioconjug. Chem.* **2011**, *22*, 1021.
[7] J. F. Lovell, T. W. Liu, J. Chen, G. Zheng, *Chem. Rev.* **2010**, *110*, 2839.
[8] a) J. F. Lovell, G. Zheng, *J. Innovative Opt. Health Sci.* **2008**, *1*, 45; b) K. Stefflova, J. Chen, G. Zheng, *Curr. Med. Chem.* **2007**, *14*, 2110; c) K. Stefflova, J. Chen, G. Zheng, *Front. Biosci.* **2007**, *12*, 4709.
[9] a) M. Dong, W. H. Tepp, E. A. Johnson, E. R. Chapman, *Proc. Natl. Acad. Sci. U. S. A.* **2004**, *101*, 14701; b) J. Lin, Z. Zhang, J. Yang, S. Zeng, B. F. Liu, Q. Luo, *J. Biomed. Opt.* **2006**, *11*, 024011; c) J. Lu, Z. Zhang, J. Yang, J. Chu, P. Li, S. Zeng, Q. Luo, *Biochem. Biophys. Res. Commun.* **2007**, *362*, 25; d) Z. Zhang, J. Yang, J. Lu, J. Lin, S. Zeng, Q. Luo, *J. Biomed. Opt.* **2008**, *13*, 011006; e) J. Chen, K. Stefflova, M. J. Niedre, B. C. Wilson, B. Chance, J. D. Glickson, G. Zheng, *J. Am. Chem. Soc.* **2004**, *126*, 11450; f) G. Zheng, J. Chen, K. Stefflova, M. Jarvi, H. Li, B. C. Wilson, *Proc. Natl. Acad. Sci. U. S. A.* **2007**, *104*, 8989; g) P. C. Lo, J. Chen, K. Stefflova, M. S. Warren, R. Navab, B. Bandarchi, S. Mullins, M. Tsao, J. D. Cheng, G. Zheng, *J. Med. Chem.* **2009**, *52*, 358; h) J. Chen, T. W. Liu, P. C. Lo, B. C. Wilson, G. Zheng, *Bioconjug. Chem.* **2009**, *20*, 1836; i) T. M. Mawn, A. V. Popov, N. J. Beardsley, K. Stefflova, M. Milkevitch, G. Zheng, E. J. Delikatny, *Bioconjug. Chem.* **2011**, *22*, 2434.
[10] a) J. Chen, J. F. Lovell, P. C. Lo, K. Stefflova, M. Niedre, B. C. Wilson, G. Zheng, *Photochem. Photobiol. Sci.* **2008**, *7*, 775; b) E. Clo, J. W. Snyder, N. V. Voigt, P. R. Ogilby, K. V. Gothelf, *J. Am. Chem. Soc.* **2006**, *128*, 4200; c) I. V. Nesterova, S. S. Erdem, S. Pakhomov, R. P. Hammer, S. A. Soper, *J. Am. Chem. Soc.* **2009**, *131*, 2432; d) J. F. Lovell, J. Chen, M. T. Jarvi, W. G. Cao, A. D. Allen, Y. Liu, T. T. Tidwell, B. C. Wilson, G. Zheng, *J. Phys. Chem. B* **2009**, *113*, 3203; e) J. F. Lovell, J. Chen, E. Huynh, M. T. Jarvi, B. C. Wilson, G. Zheng, *Bioconjug. Chem.* **2010**, *21*, 1023.
[11] a) J. Arnbjerg, M. Johnsen, C. B. Nielsen, M. Jorgensen, P. R. Ogilby, *J. Phys. Chem. A* **2007**, *111*, 4573; b) Y. Vakrat-Haglili, L. Weiner, V. Brumfeld, A. Brandis, Y. Salomon, B. McLlroy, B. C. Wilson, A. Pawlak, M. Rozanowska, T. Sarna, A. Scherz, *J. Am. Chem. Soc.* **2005**, *127*, 6487; c) S. O. McDonnell, M. J. Hall, L. T. Allen, A. Byrne, W. M. Gallagher, D. F. O'Shea, *J. Am. Chem. Soc.* **2005**, *127*, 16360; d) T. Yogo, Y. Urano, A. Mizushima, H. Sunahara, T. Inoue, K. Hirose, M. Iino, K. Kikuchi, T. Nagano, *Proc. Natl. Acad. Sci. U. S. A.* **2008**, *105*, 28.
[12] a) J. R. McCarthy, J. M. Perez, C. Bruckner, R. Weissleder, *Nano Lett.* **2005**, *5*, 2552; b)H. Ding, B. D. Sumer, C. W. Kessinger, Y. Dong, G. Huang, D. A. Boothman, J. Gao, *J. Controlled Release* **2011**, *151*, 271.
[13] J. F. Lovell, C. S. Jin, E. Huynh, H. Jin, C. Kim, J. L. Rubinstein, W. C. Chan, W. Cao, L. V. Wang, G. Zheng, *Nat. Mater.* **2011**, *10*, 324.
[14] a) J. F. Lovell, C. S. Jin, E. Huynh, T. D. MacDonald, W. Cao, G. Zheng, *Angew. Chem. Int. Ed. Engl.* **2012**, *51*, 2429; b) C. S. Jin, J. F. Lovell, G. Zheng, J Vis Exp **2013**, 79, e50536.
[15] T. W. Liu, T. D. MacDonald, J. Shi, B. C. Wilson, G. Zheng, *Angew. Chem. Int. Ed. Engl.* **2012**, *51*, 13128.
[16] A. C. Antony, *Blood* **1992**, *79*, 2807.
[17] J. Sudimack, R. J. Lee, *Adv. Drug Delivery Rev.* **2000**, *41*, 147.
[18] S. D. Weitman, R. H. Lark, L. R. Coney, D. W. Fort, V. Frasca, V. R. ZurawskiJr, B. A. Kamen, *Cancer Res.* **1992**, *52*, 3396.
[19] C. M. Paulos, M. J. Turk, G. J. Breur, P. S. Low, *Adv. Drug Delivery Rev.* **2004**, *56*, 1205.
[20] A. R. Hilgenbrink, P. S. Low, *J. Pharm. Sci.* **2005**, *94*, 2135.
[21] a) R. J. Lee, P. S. Low, *J. Biol. Chem.* **1994**, *269*, 3198; b) M. J. Turk, D. J. Waters, P. S. Low, *Cancer Lett.* **2004**, *213*, 165; c) A. Gabizon, H. Shmeeda, A. T. Horowitz, S. Zalipsky, *Adv. Drug Delivery Rev.* **2004**, *56*, 1177.
[22] C. S. Jin, J. F. Lovell, J. Chen, G. Zheng, *ACS Nano* **2013**, *7*, 2541.
[23] G. Xiang, J. Wu, Y. Lu, Z. Liu, R. J. Lee, *Int. J. Pharm.* **2008**, *356*, 29.
[24] H. Shmeeda, L. Mak, D. Tzemach, P. Astrahan, M. Tarshish, A. Gabizon, *Mol. Cancer Ther.* **2006**, *5*, 818.
[25] A. Gabizon, A. T. Horowitz, D. Goren, D. Tzemach, H. Shmeeda, S. Zalipsky, *Clin. Cancer Res.* **2003**, *9*, 6551.
[26] M. Wang, M. Thanou, *Pharmacol. Res.* **2010**, *62*, 90.
[27] E. Huynh, G. Zheng, *Wiley Interdiscip. Rev. Nanomed. Nanobiotechnol.* **2013**, *5*, 250.
[28] T. W. Liu, T. D. Macdonald, C. S. Jin, J. M. Gold, R. G. Bristow, B. C. Wilson, G. Zheng, *ACS Nano* **2013**, *7*, 4221.

A PEGylation-Free Biomimetic Porphyrin Nanoplatform for Personalized Cancer Theranostics

Liyang Cui,[†,‡,§] Qiaoya Lin,[†,⊥] Cheng S. Jin,[†,∥,#] Wenlei Jiang,[†] Huang Huang,[†] Lili Ding,[†] Nidal Muhanna,[†,▽] Jonathan C. Irish,[†,▽] Fan Wang,[§] Juan Chen,[*,†] and Gang Zheng[*,†,‡,∥,#]

[†]Princess Margaret Cancer Centre and Techna Institute, University Health Network, Toronto, Ontario M5G 2M9, Canada, [‡]Department of Medical Biophysics, University of Toronto, Toronto, Ontario M5S 2J7, Canada, [§]Medical Isotopes Research Center, Peking University, Beijing 100871, China, [⊥]Britton Chance Center for Biomedical Photonics, Wuhan National Laboratory for Optoelectronics, Huazhong University of Science & Technology, Wuhan 430074, China, [∥]Department of Pharmaceutical Sciences, Leslie Dan Faculty of Pharmacy, University of Toronto, Toronto, Ontario M5S 2J7, Canada, [#]Institute of Biomaterials and Biomedical Engineering, University of Toronto, Toronto, Ontario M5S 2J7, Canada, and [▽]Otolaryngology — Head and Neck Surgery, University of Toronto, Toronto, Ontario M5S 2J7, Canada

ABSTRACT PEGylation (PEG) is the most commonly adopted strategy to prolong nanoparticles' vascular circulation by mitigating the reticuloendothelial system uptake. However, there remain many concerns in regards to its immunogenicity, targeting efficiency, *etc.*, which inspires pursuit of alternate, non-PEGylated systems. We introduced here a PEG-free, porphyrin-based ultrasmall nanostructure mimicking nature lipoproteins, termed PLP, that integrates multiple imaging and therapeutic functionalities, including positron emission tomography (PET) imaging, near-infrared (NIR) fluorescence imaging and photodynamic therapy (PDT). With an engineered lipoprotein-mimicking structure, PLP is highly stable in the blood circulation, resulting in favorable pharmacokinetics and biodistribution without the need of PEG. The prompt tumor intracellular trafficking of PLP allows for rapid nanostructure dissociation upon tumor accumulation to release monomeric porphyrins to efficiently generate fluorescence and photodynamic reactivity, which are highly silenced in intact PLP, thus providing an activatable mechanism for low-background NIR fluorescence imaging and tumor-selective PDT. Its intrinsic copper-64 labeling feature allows for noninvasive PET imaging of PLP delivery and quantitative assessment of drug distribution. Using a clinically relevant glioblastoma multiforme model, we demonstrated that PLP enabled accurate delineation of tumor from surrounding healthy brain at size less than 1 mm, exhibiting the potential for intraoperative fluorescence-guided surgery and tumor-selective PDT. Furthermore, we demonstrated the general applicability of PLP for sensitive and accurate detection of primary and metastatic tumors in other clinically relevant animal models. Therefore, PLP offers a biomimetic theranostic nanoplatform for pretreatment stratification using PET and NIR fluorescence imaging and for further customized cancer management *via* imaging-guided surgery, PDT, or/and potential chemotherapy.

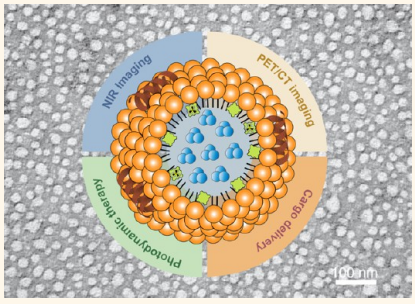

KEYWORDS: porphyrin · nanoparticle · PEGylation · PET imaging · multimodal imaging · fluorescence-guided surgery · photodynamic therapy

Personalized medicine focuses on tailoring of medical treatment to the individual characteristics, needs and preferences of patients during all stages of care from diagnosis, treatment to prognosis. Theranostic, an integrated form of imaging and therapy, plays an increasingly important role in personalized cancer treatment, where imaging modalities not only offer the potential to noninvasively detect and functionally characterize disease, but also provide a quantitative way to assess the delivery of therapy in tumor regions and specify the activation state of a therapeutically shielded drug for finely tuned treatment planning. Furthermore, multimodal imaging could provide complementary information pertaining to the strengths of the individual modalities to better elucidate disease from morphological behaviors to physiological mechanisms. Research in the development of nanoscale theranostics sits at the forefront of rapidly expanding field of cancer personalized medicine to improve solubility of functional agents, protect from premature degradation, prolong blood circulation and enhance tumor accumulation through the enhanced permeability and retention (EPR) effect,[1] and

* Address correspondence to juan.chen@uhnresearch.ca, gang.zheng@uhnres.utoronto.ca.

Received for review February 15, 2015 and accepted April 1, 2015.

Published online April 01, 2015
10.1021/acsnano.5b01077

control drug release.[2] The majority of reported multifunctional nanoparticles, including inorganic,[3−9] organic,[10−13] and the recently reported porphysome,[14] require PEG to ameliorate the stability and avoid fast clearance by reticuloendothelial system (RES) *in vivo*. Although multiple PEGylated nanoparticles have been clinically approved, there remain several concerns including "PEG dilemma" (inhibition of intracellular trafficking of nanoparticles and subsequent endosomal escape),[15−18] immunogenicity,[19,20] anti-PEG immune response,[15,21−23] biocompatibility and toxicity issues following chronic administration.[24,25] Previous attempts to solve the issues typically involve developing PEG linker-removable approaches,[26] using nonbioadhesive surface-coating materials, such as polysaccharides, poly(vinyl alcohol), and other nonbioadhesive hydrophilic polymers,[27] or hitchhiking blood cells to prolong intravascular particle circulation.[28] Lipoproteins are naturally existing nanoparticles that evade RES uptake, thus exhibiting a long circulating half-life (the native HDLs in humans have a circulating half-life of 9−15 h[29]), offering another PEG-free pathway to design biomimetic long circulating theranostic nanomedicine.[30−39] By engaging the biocompatible nanostructure of lipoprotein and the multifunctionalities of naturally derived porphyrin molecules, we developed a novel PEG-free, porphyrin-based ultrasmall nanostructure mimicking nature lipoproteins, termed porphylipoprotein (PLP), which contains a hydrophobic drug-loadable core, enveloped in porphyrin-lipid monolayer, and constrained by ApoA-1 mimetic R4F (Ac-FAEKFKEAVKDYFAKFWD) peptide networks. We demonstrated that the α-helix structure endorsed by peptide network played an essential role in constricting the size, stabilizing the particles, and the favorable pharmacokinetic behaviors *in vivo* without need of PEG. PLP nanoplatform integrates a variety of imaging and therapeutic functionalities including positron emission tomography (PET) imaging, activatable near-infrared (NIR) fluorescence and photodynamic therapy (PDT). More importantly, we demonstrated that PLP potentiated the customized cancer management on a clinically relevant glioblastoma multiforme (GBM) model. The tumor-selective activation of NIR fluorescence facilitated the delineation of tumor, providing real-time low-background intraoperative guidance for complete tumor resection. Consistently, the selectively activated photodynamic reactivity enabled potent PDT for tumor ablation and surgery bed cleaning. The general applicability of PLP for sensitive and accurate detection of primary and metastatic tumors was further demonstrated in other clinically relevant animal models.

RESULTS AND DISCUSSION

Synthesis and Characterization of PLP. PLP was formulated by assembly of porphyrin-lipid and DMPC-phospholipid on a hydrophobic core in aqueous buffered solution, followed by size-constraint with an 18-amino acid ApoA-1 mimetic peptide R4F (Figure 1a). Transmission electronic microscopy (TEM) showed a spherical structure of PLP with 20 nm in diameter (Figure 1b). At the 400 000 magnification view of TEM, a core−shell lipoprotein-mimicking structure of PLP was revealed (Figure1b, top right corner). The size distribution and ζ potential were determined by dynamic light scattering measurement, showing a monodispersed particle peak at 20.6 ± 5.2 nm (Figure S1, Supporting Information) with ζ potential of −6.07 ± 0.71 mV. A fingerprint α-helix structure of PLP was revealed by circular dichroism (CD) spectrum, manifesting the role of peptide on the control of the particle structure (Figure 1c).[40]

The photophysical properties of PLP are dependent on the proportion of porphyrin-lipid in the total phospholipid used for nanoparticle construction. Increasing the content of porphyrin-lipid led to the enhancement of porphyrin fluorescence quenching together with the increase of particle size (Figure S2). The PLP with 30 mol % of porphyrin-lipid was chosen as an optimal formulation given its high-density packing of porphyrin-lipid (fluorescence quenching efficiency >95%, Figure 1e) and favorable size (<30 nm). According to its characteristic absorption bands of porphyrin at peaks of 420 and 680 nm (Figure 1d) and the particle concentration calculated by the previously reported method for lipoprotein-like nanoparticles,[41] the estimated extinction coefficient of PLP was $\varepsilon_{680} = 7.8 \times 10^7$ cm^{-1} M^{-1}, further confirming the highly dense packing of porphyrin-lipid on PLP. Consistent with the fluorescence quenching, the photodynamic reactivity was also suppressed in intact PLP which exhibited 2−3 fold less singlet oxygen generation compared to the nanostructure-disrupted samples at a wide range of light fluence (0.5−10 J/cm^2, Figure 1f). These results suggest that the photoactivity of PLP is "switched-off" in the intact form, but can be promptly "switched-on" upon its structural disruption, thus exhibiting an activatable fashion for low background fluorescence imaging and selective PDT. In addition, taking advantage of the intrinsic metal chelation capacity of porphyrin, PLP can be directly labeled with radionuclide copper-64 through a robust one-pot procedure to attain ^{64}Cu-PLP with high yield (97.5 ± 1.8%, $n = 5$) and high stability (93.8 ± 2.1%, $n = 5$) within 24 h storage (the methods for measuring labeling efficiency and stability are available in the Supporting Information).

Pharmacokinetics of PLP. The α-helix peptide network not only facilitated the constraint of PLP size, but also stabilized the nanostructure under physiological condition. As shown in Figure 1g, PLP remained highly fluorescence-quenched either in stock PBS at 4 °C (98.4%) or in PBS containing 10% FBS at 37 °C (97.0%) for 24 h, indicating insignificant occurrence of particle dissociation. The pharmacokinetic profile of

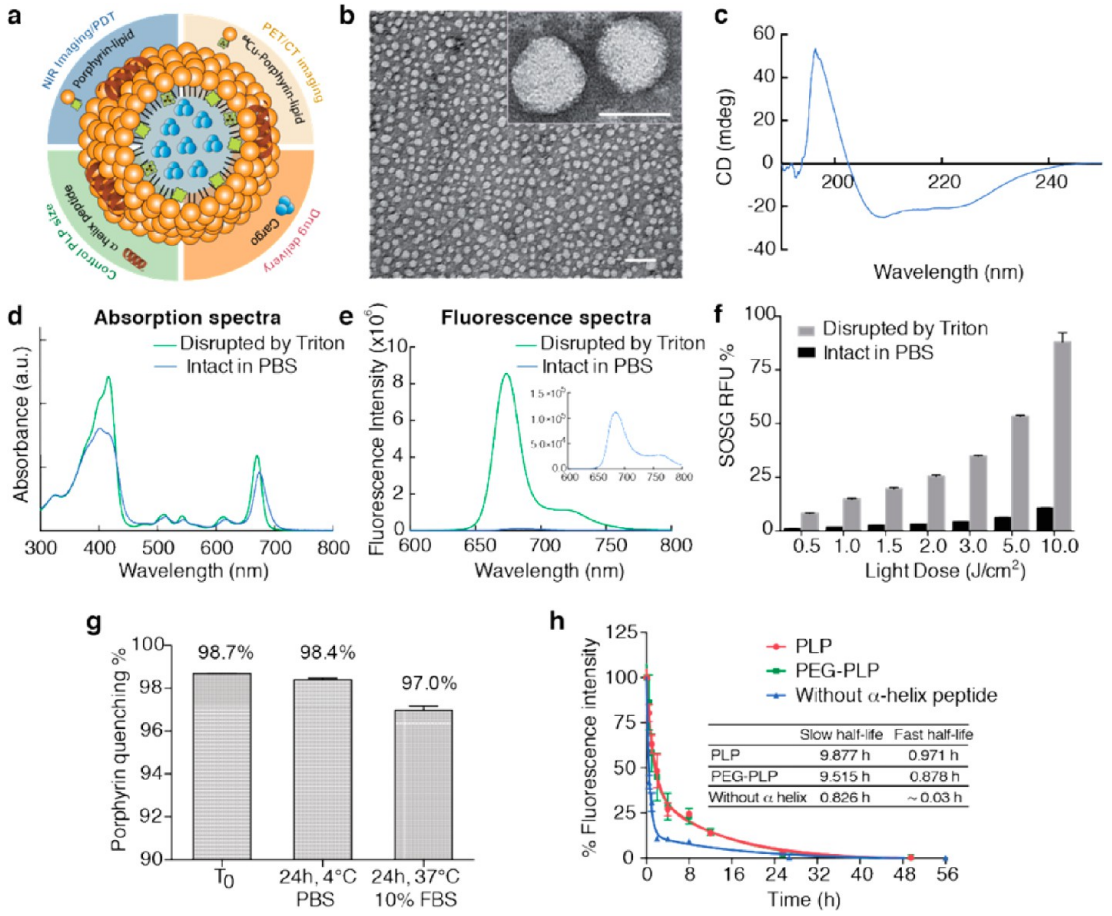

Figure 1. The scheme and characterization of PLP. (a) Schematic of PLP structure. (b) TEM showed a core−shell spherical structure of PLP with size around 20 nm (the scales represented 100 and 20 nm respectively, for the whole view and the magnified view). (c) Circular dichroism spectrum of PLP, affirming the α-helix structure assembled on the particle. (d) UV−vis absorption spectra of intact (blue) and nanostructure-disrupted (green) PLPs. (e) Fluorescence emission spectra of intact (blue) and disrupted (green) PLPs. (f) Singlet oxygen generation of intact and disrupted PLP upon laser irradiation at light dose from 0.5 to 10 J/cm^2 measured by singlet oxygen sensor green (SOSG) assay. (g) Stability of PLP monitored by the change of porphyrin fluorescence quenching efficiency under different condition: the freshly prepared PLP (T_0); the sample stored for 24 h at 4 °C in PBS; and the sample incubated at 37 °C in 10% FBS for 24 h. (h) Blood clearance curve of PLP (red, n =5), PEGylated PLP (green, n =5) and PLP formulation without α-helix (blue n = 4) in mice. The profiles fit into the two-compartment model with slow half-life of 9.88 h for PLP and 9.52 h for PEGylated PLP.

PLP showed a favorable slow half-life (9.9 h) similar to that of PEGylated PLP (containing 5 mol % of PEG-lipid) with half-life of 9.5 h (Figure 1h). However, without the α-helix peptide, the particle dissociated very quickly in the bloodstream showing a slow half-life of 0.83 h only. These results suggested that the α-helix peptide plays a key role in stabilizing nanoparticles to provide PEG-free PLP a favorite circulation time comparable to that of PEGylated PLP, thus excluding the need of PEG for favoring the pharmacokinetics of PLP. Therefore, PLP has confirmed to mimic not only the structure of lipoproteins, but also their biological behaviors to circulate in the bloodstream with a favorite half-life.

Fast Fluorescence and Photodynamic Activation of PLP. Compared with the previously reported liposome-like porphysomes, the PEG-free, ultrasmall, α-helix structured PLP showed significantly enhanced intracellular uptake in cancer cells. As shown in Figure 2a, PLP exhibited 10 times higher uptake than porphysome in U87 cancer cells after 3 h incubation with the same concentration of porphyrin. In addition, unlike the fluorescence activation of porphysome in cell experienced a time-consuming process,[14,42] PLP exhibited rapid activation of porphyrin fluorescence in cells without showing gradual increase of fluorescence after incubation (Figure 2b,c). These data implied that the PLP nanostructure facilitated not only the tumor intracellular uptake, but also fast fluorescence activation.

The *in vivo* behaviors of these two particles were further compared in the SKOV3 orthotopic ovarian cancer model by using their ^{64}Cu-labled versions. As shown in Figure 2d, PLP exhibited very similar biodistribution as PEGylated porphysome, but displayed notably lower spleen uptake than porphysome (3.4 ± 0.2% ID/g *versus* 19.8 ± 1.6% ID/g, n = 3, P < 0.01), fitting to the biodistribution pattern observed for lipoprotein-like nanoparticles.[41] Although the two nanoparticles displayed similar tumor accumulation

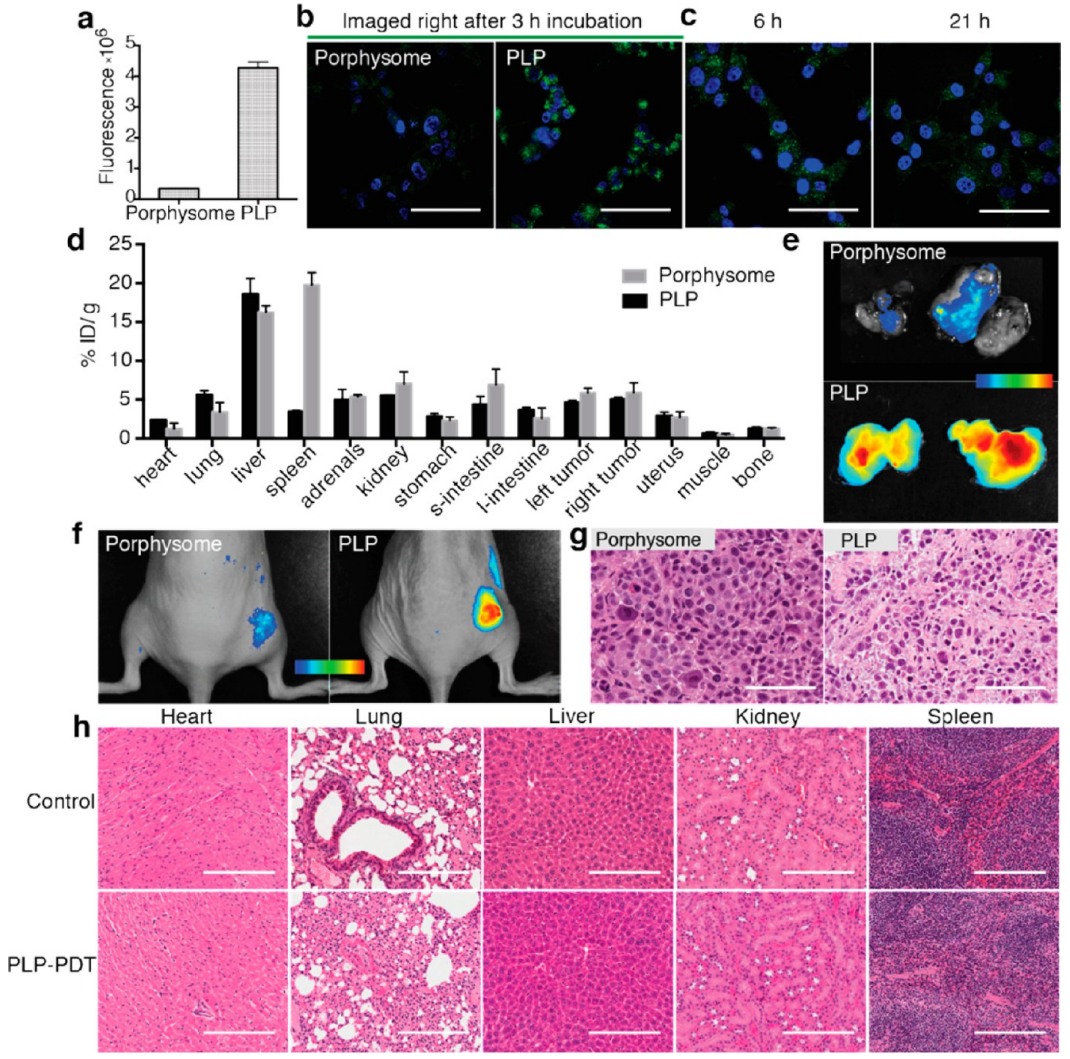

Figure 2. PLP enabled fast activation of fluorescence and photodynamic activity. (a) Comparing the cell uptake of porphysome and PLP in U87 cells by measuring the porphyrin fluorescence of the corresponding cell lysate (n = 3, P < 0.05). (b) Confocal images of U87 cells right after 3 h incubation with porphysome or PLP. (c) Consecutive confocal imaging of the PLP-incubated cells at 6 and 21 h after 3 h incubation. Scale bar in (b) and (c) was 50 μm. (d) Biodistribution of ^{64}Cu-porphysome and ^{64}Cu-PLP in SKOV3 orthotopic ovarian cancer model (n = 3, mean ± SEM) quantified by γ-counting assay. (e) Representative *ex vivo* fluorescence images of the exercised orthotopic SKOV3 tumors from ^{64}Cu-porphysome and ^{64}Cu-PLP porphysome dosed mice, respectively. (f) *In vivo* fluorescence activation of porphysome *versus* PLP in KB-xenograft model at 24 h after intravenous injection. (g) H&E staining of tumor sections at 24 h after porphysome-PDT and PLP−PDT (scale bar: 50 μm). (h) H&E staining of hearts, lungs, livers, kidneys and spleens from mice with or without conducting PLP−PDT treatment (scale bar: 200 μm).

based on γ-counting, PLP exhibited much higher fluorescence in tumor compared to porphysome under *ex vivo* fluorescence imaging (Figure 2e), confirming the rapid fluorescence activation of PLP *in vivo*. We next investigated if the suppressed photodynamic reactivity of PLP could also be quickly activated in tumors. After 24 h administration of PLP or porphysome with the same porphyrin dose, it is unsurprised to find that the KB-xenograft mice administrated with PLP displayed much stronger tumor fluorescence than porphysome-dosed ones (Figure 2f). The fluorescent tumors then received localized laser treatment (671 nm, 100 mW/cm^2, 75 J/cm^2), and the treatment efficacy was examined by H&E histological analysis at 24 h post-PDT. As shown in Figure 2g, PLP−PDT group showed clear tumor cellular damage while porphysome-PDT group gave negligible effect, suggesting that PLP enabled a fast photodynamic activation in tumors for selective and effective PDT. In addition, no obvious cellular damage and morphology change were observed in the healthy organs of PLP−PDT groups compared to blank control (Figure 2h), indicating that the PLP−PDT is a safe treatment approach.

Theranostics Application of PLP for GBM Management. Efficient delivery of imaging and therapeutic agents into intracerebral region remains a major challenge in GBM management. Conventional therapeutic agents are often blocked by the blood-brain barrier (BBB) and

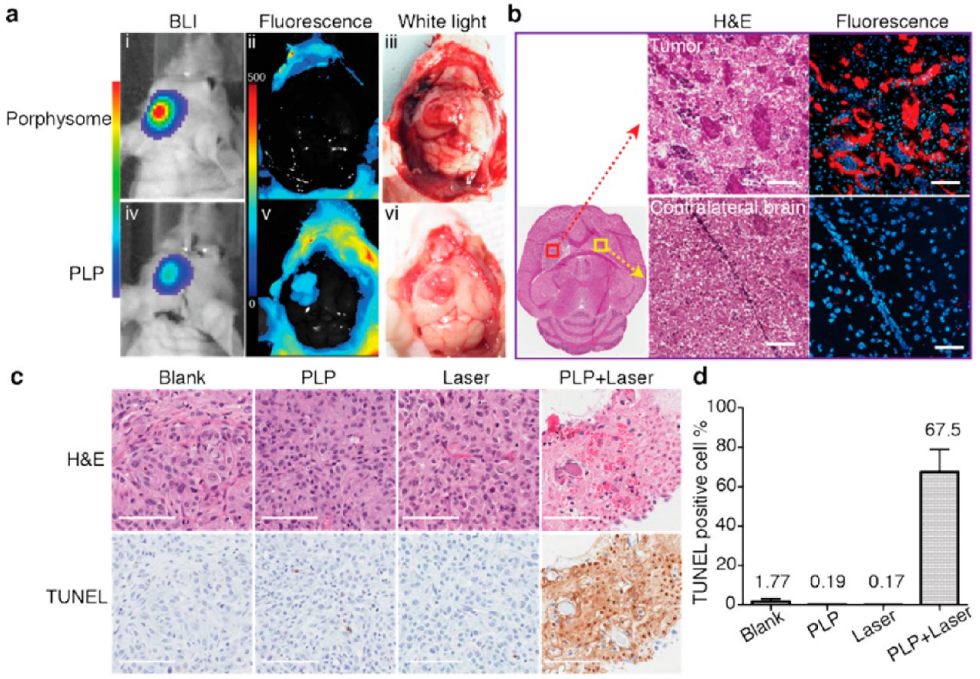

Figure 3. Tumor-specific accumulation and PDT activation of PLP in glioma. (a) Intraoperative bioluminescence, fluorescence and white light images of 9L^{luc} glioma-bearing mice under the crania opening after 24 h injection of porphysomes and PLP. (b) Representative H&E staining image of brain from PLP-administrated mice, with the magnified images showed the corresponding H&E staining and fluorescence microscopic imaging (blue: DAPI, red: porphyrin) of the tumor region and contralateral healthy brain region (scale bar: 100 μm). (c) Representative H&E and TUNEL staining of glioma tumor sections from the blank control, laser alone control, PLP alone control and PLP−PDT group at 24 h post-PDT (scale bar: 100 μm). (d) Quantitative analysis of TUNEL positivity out of whole tumor region in the four groups (n = 3).

cannot access to the glioma cells. Even in the BBB-compromised case, other obstacles, such as the brain blood tumor barrier and the dynamic force caused by the cerebrospinal fluid, hinder the effective drug delivery upon systematic administration.[43,44] Here we assessed the theranostic potential of PLP in a clinically relevant GBM model. The results in Figure 3a demonstrated that PLP significantly accumulated in tumor of the 9L^{luc} gliosarcoma mice with high fluorescence of tumor against the nonfluorescent surrounding healthy brain. The detected PLP fluorescence (Figure 3a-v) was well colocalized with the tumor bioluminescence (BLI) signal (Figure 3a-iv) and with the visualized tumor tissue under the crania opened view (Figure 3a-vi). In contrast, porphysome-dosed animals showed negligible tumor fluorescence under the same imaging setting (Figure 3a-ii), demonstrating the superiority of PLP in brain tumor delivery and detection. When comparing fluorescence microscopic imaging and H&E image of the PLP-dosed brain tissue slides, strong porphyrin fluorescence was observed only in tumor region, but not in the contralateral brain (Figure 3b), further validating the tumor specific uptake of PLP.

In observation of significant fluorescence activation of PLP in glioma tumor, we expected efficient PDT activity as well. Four groups, including blank control, laser control, PLP control and PLP−PDT (PLP + Laser) group, were employed to evaluate the PDT efficacy of PLP. At 24 h postinjection, PLP−PDT group was subjected to trans-cranium laser irradiation (671 nm, 50 mW/cm^2, 50 J/cm^2) (a detailed procedure on trans-skull PDT is available in the Supporting Information). Minimal temperature increase during the treatment excluded the thermal effect (Figure S3a). The PDT efficacy was evaluated by *postmortem* histopathological analysis. PLP−PDT group displayed condensed nuclei and loss of cell structure in tumor while control groups did not (Figure 3c). TUNEL staining analysis further revealed that PLP−PDT induced significant tumor cell apoptosis (67.5 ± 11.4%), while the controls showed minimal tumor apoptosis (1.77 ± 1.37% for blank, 0.17 ± 0.05% for laser control and 0.19 ± 0.07% for PLP control) (Figure 3d). Moreover, the adjacent healthy brain after PLP-PDT showed none of cellular damage, morphology change and cell apoptosis (Figure S3b), demonstrating the high selectivity of PLP−PDT to tumors. Therefore, PLP−PDT could be an appealing alternative[45] to current radiation treatment for treating GBM subtypes that are not surgically accessible or for cleaning the surgery bed after operative procedure.[46]

Stable Delivery of PLP into GBM. In observation of rapid fluorescence and photodynamic activation of PLP in GBM, we next experimented to investigate if PLP remained stable during the systemic delivery. The core−shell structure of PLP allowed for loading of a NIR hydrophobic dye, DiR-BOA, in the particle core without compromising the particle structure and optical properties (Figure S4), thus providing a dual

fluorescence labeled PLP (core labeled with DiR-BOA and shell labeled with porphyrin) to track the particle integrity during systemic delivery. The CRI Maestro hyperspectral imaging system equipped with yellow filter (Ex. 575−605 nm, Em: 645−730 nm) and NIR filter (Ex: 725−755 nm, Em: 780 nm long-pass) was used to monitor porphyrin and DiR-BOA fluorescence, respectively. At 24 h post-administration of PLP(DiR-BOA) in orthotopic U87 glioma bearing mice, brain tumor margin was clearly delineated from surrounding healthy brain by both porphyrin and DiR-BOA fluorescence. The remarkable colocalization of two fluorescence signals suggested that PLP maintained integrity during the systemic delivery and allowed for a stable and efficient delivery of both shell and core components into tumor *in vivo* (Figure 4a). Notably, the *ex vivo* tissue fluorescence imaging (Figure S5) further confirmed the well-matched porphyrin and DiR-BOA signals in most of organs, demonstrating the integrity of PLP during the blood circulation within 24 h. Therefore, the observed rapid fluorescence and photodynamic activation of PLP in tumor were likely happened after the entire particles accumulation, excluding the concern of premature degradation of PLP.

PLP for Intraoperative Fluorescence-Guided Surgery of GBM. Surgical removal of the tumors remains the mainstream of GBM treatment prior to other treatments in clinic, but it experienced major challenge on precise delineation positive margins for sufficient surgery while maintaining important neuro-functions.[47,48] PLP demonstrated its stable systemic delivery and its ability for delineation of tumor from surrounding healthy brain by the activated porphyrin fluorescence. Even at microscopic level, it allowed for highly sensitive detection of tumor by an *in vivo* confocal microscopy (Figure 4b), separating completely from the nonfluorescent contralateral brain tissue. We therefore investigated PLP as fluorescent intraoperative guide for brain tumor surgery. Orthotopic $U87^{GFP}$ glioma mice with tumor deeply seeded inside brain (over 5 mm deep from top surface, identified by MRI in Figure 4c-ii) were used to mimic clinical scenario. At 24 h after injection of PLP(DiR-BOA), both intrinsic porphyrin fluorescence and DiR-BOA fluorescence could be detected by fluorescence molecular tomography (FMT) imaging system in glioma mice (Figure 4c-iii), while neither was detected in the brain of sham control (mice received the same surgical procedure as the glioma mice but had saline injection instead of tumor cells) (Figure S6), eliminating the possibility of false-positive uptake of PLP related to tumor-induction surgery. As illustrated in Figure 4d, the brain was subjected to the coronal transection to remove the top portion with minimal malignancy (negligible GFP signal of tumor) and to expose the major solid tumor (strong GFP signal of tumor) in the bottom portion. The tumor and malignant peripheral region were clearly delineated by both porphyrin and DiR-BOA fluorescence and the two signals were well-correlated with the tumor GFP signal (Figure 4e). Guided with the porphyrin fluorescence, the suspicious malignancy was surgically removed and the final surgery bed exhibited minimal porphyrin and GFP fluorescence, implying the completion of tumor resection. The resected tissues were confirmed malignant by histological analysis and displayed the well-matched porphyrin fluorescence and tumor GFP signal under fluorescence microscopy (Figure S7), indicating that PLP was able to detect primary tumor at cellular level to precisely guide the surgery. Malignant gliomas sometimes occur within multiple compartments in the brain and lead to the failure in the gross total resection.[49] PLP demonstrated the ability to identify multiple foci of $U87^{luc}$ tumors that scattered through the mice brain ranging from 4 mm to less than 1 mm in size with matched porphyrin fluorescence and tumor BLI signal (Figure 4f). Given that surgical outcome is critical for GBM management and prognosis, PLP fluorescence-guided tumor dissection presented a promising add-on to facilitate the standard surgery procedure.

Multimodal Imaging Application of PLP on Other Cancer Models. Beyond the GBM application, we further evaluated the theranostic applicability of PLP in other types of primary and metastatic tumor animal models. After 24 h injection of ^{64}Cu-PLP with the radioactivity of 43 Ci per μmol of particle, the deep-seated PC-3 orthotopic prostate tumor was clearly delineated in both axial and coronal views of coregistered PET and computed tomography (CT) images (Figure 5a). The tumor-selective accumulation was quantitatively confirmed by γ-counting assay, which revealed significantly higher PLP accumulation in tumor (5.27 $\pm$ 0.48% ID/g) *versus* healthy prostate (1.95 $\pm$ 0.81% ID/g) (n = 4, P < 0.05, Figure 5b). Meantime, significantly higher fluorescence was observed in tumor over the surrounding organs (Figure 5c) under *ex vivo* tissue imaging. On the basis of the high fluorescence contrast of tumor/nontumor, nonradioactive PLP was then explored for fluorescence-guided intervention of primary prostate tumor. At 24 h postinjection of 10 mg/kg of PLP, the orthotopic tumor was depicted noninvasively by imaging coregistration of CT and FMT, suggesting that the activated inherent fluorescence of PLP enabled preoperative assessment of prostate orthotopic tumor (Figure 5d). The fluorescent region under FMT/CT view was surgically exposed and the tumor in pelvic cavity was clearly demarcated under intraoperative fluorescence imaging (Figure 5e-i). Guided with the porphyrin fluorescence, the suspicious tumor tissue was resected. The clean surgical bed (Figure 5e-ii) after tumor removal validated the tumor-preferential accumulation and activation of PLP.

The multimodal cancer imaging by PLP was further evaluated in a luciferase-expressing metastatic tumor

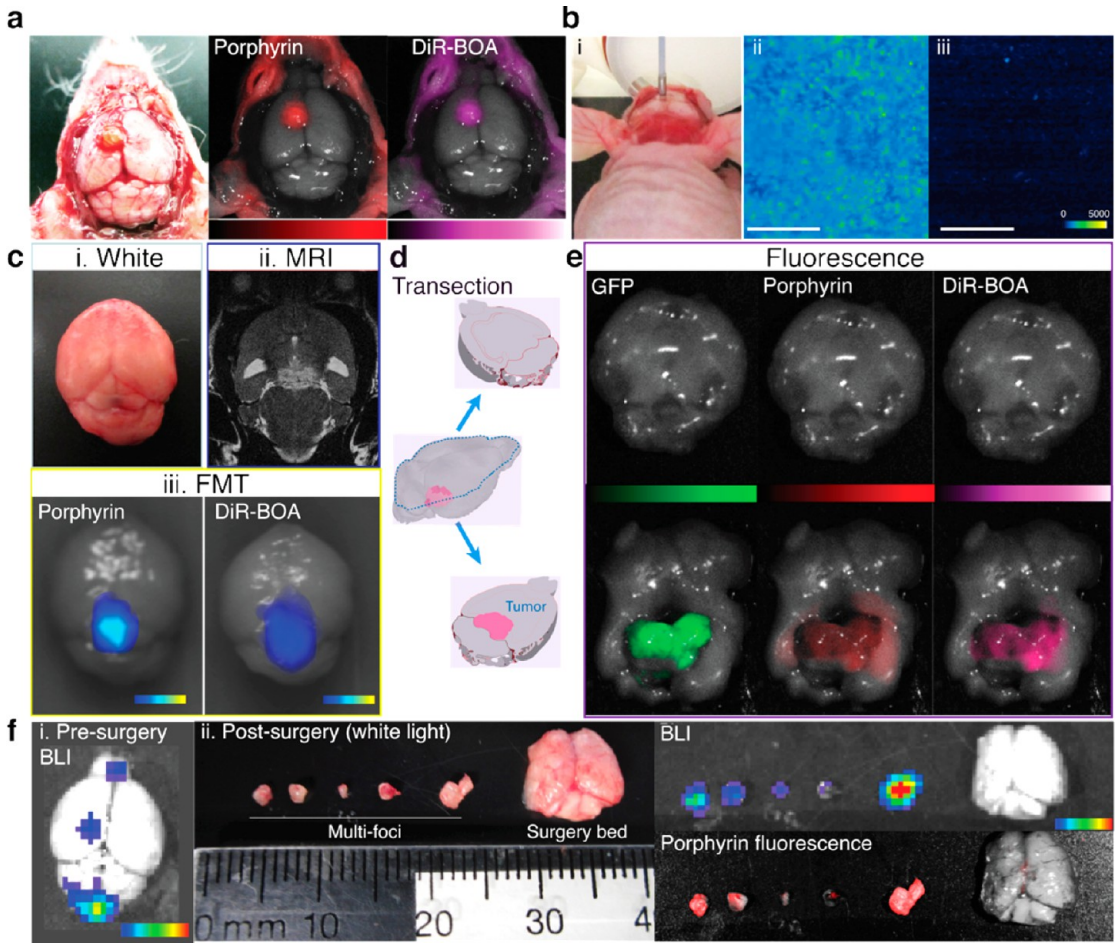

Figure 4. Image-guided intervention of glioblastoma multiforme by PLP. (a) Photograph image and the corresponding porphyrin and DiR-BOA fluorescence images of the brain from the orthotopic U87^{GFP} glioma mice at 24 h post-injection of PLP(DiR-BOA). (b) Representative *in vivo* fluorescence microscopic images of tumor (ii) and contralateral brain (iii) obtained with deep red long-pass laser probe (i) under the crania opening (the scales in both b(ii) and b(iii) are 100 μm). (c) The entire brains with deep-seeded U87^{GFP} tumor were imaged by photograph image (i); MRI (ii); and FMT (iii) at 24 h postinjection of PLP(DiR-BOA). Followed the transection procedure illustrated in (d), the two separated portions were subjected to CRI Maestro hyperspectral imaging system to detect GFP signal (tumor cells), porphyrin signal (PLP), and DiR-BOA signal (cargo) (e). (f) Multifoci glioma detected by PLP. (i) Bioluminescence image of the entire U87^{luc} tumor-bearing brain. (ii) Photography, bioluminescence and porphyrin fluorescence images of multifoci resection.

model. As shown in Figure 6a, two bright hot spots were detected clearly against the low-background abdomen by ^{64}Cu-PLP enabled PET/CT imaging. The suspicious metastatic ovaries, uterus and muscle were then harvested for *ex vivo* BLI and fluorescence imaging. As shown in Figure 6b, the metastatic tumor displayed strong and well-correlated fluorescence and BLI signals whereas the muscle and connective healthy uterus showed negligible signal. The regions displayed all three signals (radioactivity, fluorescence and BLI) were further confirmed metastasis through both histopathological analysis that showed cancer cell morphology (*e.g.*, enlarged nuclei, prominent nucleoli and irregular shape), and high positive pan-cytokeratin staining (PanCK) that indicated the presence of carcinoma (Figure 6c). Therefore, PLP could specifically accumulate in both primary and metastatic tumors. This selectivity together with the intrinsic multimodal imaging capacities makes PLP an ideal tracer for tumor diagnosis and image-guided interventions.

Inspired by the nature's nanoparticles, lipoproteins, PLP opens a new avenue for designing PEG-free nanomedicine. The α-helical peptide networks not only enable stable assembly of the multifunctional components within an ultrasmall sized structure, but also render prolonged pharmacokinetic profile, favorable biodistribution, and superior intracellular trafficking. The built-in porphyrin assembly offers the coalition of multiple imaging and therapeutic functions. The natural metal chelating property of porphyrin makes PLP versatile for nuclear medicine. The intrinsic copper-64 labeling allows for noninvasive tracking PLP delivery and essentially accurate and sensitive detection of both primary tumor and metastasis by PET/CT imaging. Other metal ions, such as paramagnetic Mn or Pd, could also be incorporated into porphyrin molecules to provide an additional MRI contrast or to enhance

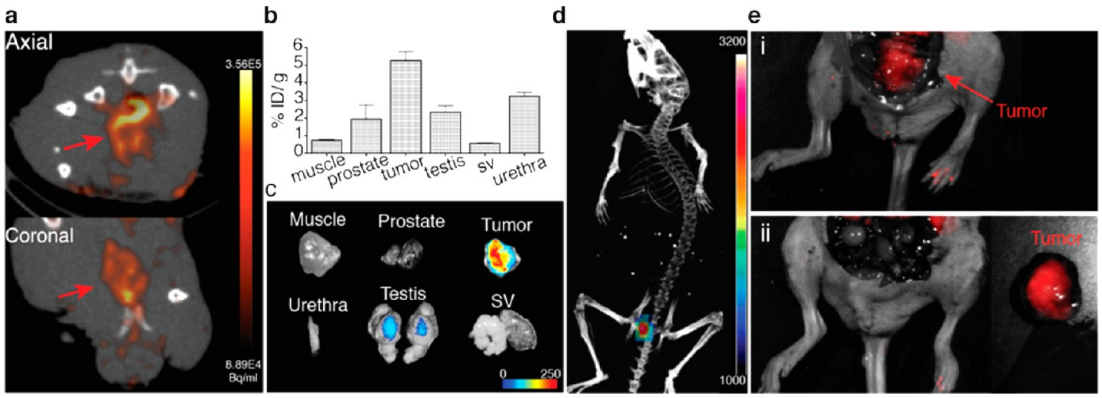

Figure 5. Tumor-specific uptake and multimodal imaging of PLP in orthotopic prostate cancer model. (a) Representative axial and coronal views of PET/CT imaging of PC-3 orthotopic prostate cancer mice after 24 h intravenous injection of ^{64}Cu-PLP (red arrow: tumor). (b) Distribution of ^{64}Cu-PLP in tumor and surrounding tissues calculated as percentage of the injected dose per gram (% ID/g), sv stands for seminal vesicle (n = 4, P < 0.05). (c) *Ex vivo* fluorescence imaging of resected tumor and surrounding tissues. (d) Representative coregistration of CT and fluorescence molecular tomography (FMT) in the region of interest after 24 h intravenous injection of PLP, clearly revealing the tumor margin. (e) Intraoperative fluorescence imaging enabling the guidance of PC-3 orthotopic tumor resection: (i) before and (ii) after resection.

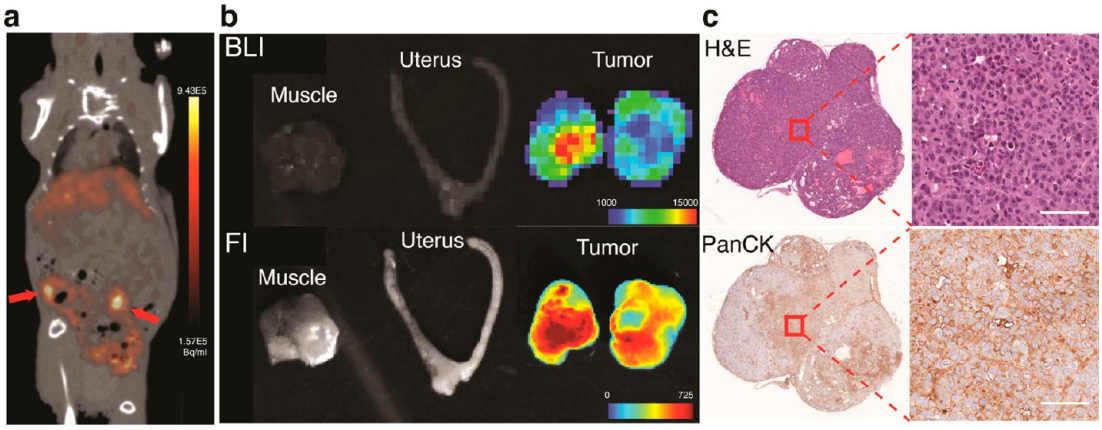

Figure 6. Ovarian cancer metastasis detected by ^{64}Cu-PLP. (a) Representative whole-body PET/CT image of mouse with ovarian cancer metastasis after 24 h intravenous injection of ^{64}Cu-PLP (red arrow: tumor). (b) *Ex vivo* bioluminescence imaging (BLI) and fluorescence imaging (FI) of metastatic tumors, uterus and muscle. (c) The PLP-detected metastases were affirmed by histopathological analysis, showing cancer cell morphology in H&E staining and pan-cytokeratin (PanCK)-positive, (the scale bar in the magnified image: 100 μm).

PDT treatment.[50] The superior PLP intracellular trafficking results in rapid and efficient activation of porphyrin fluorescence and photodynamic reactivity that were both inhibited in intact PLP, thus exhibiting an activatable mechanism for low background fluorescence imaging and tumor-selective PDT. Moreover, the core−shell lipoprotein-mimicking structure of PLP may provide amiable environment for stable delivery of drugs, such as siRNA[51−54] and hydrophobic chemotherapeutics[55−57] for personalized treatment or as adjuvant therapy for synergistic treatment. It should be noted that PLP is distinctively different from our previously reported porphysome in its nanostructure (20 nm *versus* 100 nm, monolayer *versus* bilayer, hydrophobic core *versus* aqueous core, α-helical peptide *versus* PEG coating) and nanostructure-dependent functions (fast *versus* slow intracellular trafficking, photodynamic therapy *versus* photothermal therapy).[14,58]

Although nanosized theranostics exhibits preferential accumulation in malignant tumors through the EPR effect, most of them experience hindrance to sufficient penetration within tumor. Recent studies have demonstrated that nanoparticles with size less than 40 nm was advantageous over larger-sized nanoparticles in efficient penetration into the tumor types that are poorly permeable and highly fibrotic or desmoplastic.[59−61] The PLP owns a favorable size (∼20 nm) for circumvention of fast elimination by kidneys[62] (>5 nm) and for superior diffusion through the tumor interstitium (<40 nm), thus holding great potential for improving drug delivery, especially in tumors with low permeability, such as pancreatic cancer. Though PLP (∼20 nm) and larger-sized porphysome (∼100 nm) exhibited similar tumor accumulation in the SKOV3 orthotopic tumor (Figure 2d), a significant difference was observed for their porphyrin photoreactivity activation (Figure 2e), which indicated that

the small size of PLP might promote its intratumoral transportation, along with its enhanced intracellular trafficking (Figure 2a), leading to sufficient and active porphyrin concentration in tumor cell for high-contrast fluorescence imaging and potent PDT.

Nanotoxicity is one of the general concerns in translation of nanoparticles into clinical practice.[63] Due to the natural chlorophyll origin, porphyrin-based nanoparticles were found biocompatible and biodegradable and had minimal toxicity *in vivo*.[14] Lipoproteins are naturally endogenous protein−lipid nanocomplexes essential for the regulation of lipid metabolism and cholesterol transportation.[64] Lipoprotein-mimicking nanoplatform has been demonstrated with minimal acute toxicity at a dose up to 2000 mg/kg.[56] By engaging the biocompatible nanostructure of lipoprotein and the multifunctional porphyrin molecules, PLP is able to fulfill "the one particle to rule them all" strategy for personalized medicine, sparing from the complexity, immunogenicity and toxicity issues caused by simple piling of different functional moieties. Indeed, PLP administration and PLP−PDT caused no detectable functional or histological side effects on normal tissues. The intrinsic multimodal and biomimetic nature of PLP confers high potential for cancer theranostics and clinical translation.

CONCLUSIONS

The PEG-free lipoprotein-mimicking structure of PLP conferred great biocompatibility and *in vivo* behaviors. With the built-in porphyrin, PLP exhibited intrinsically multimodal imaging and therapeutic functionalities. The inherent activatable NIR fluorescence and metal chelation enabled PET imaging provided comprehensive information for early diagnosis, disease staging, intraoperative guidance, and quantitative assessment of drug delivery. Together with the potent PDT competency, PLP allowed for the tuning of patient treatment *via* imaging-guided surgery and effective PDT.

METHODS

Materials. 1,2-Dimyristoyl-*sn*-glycero-3-phosphocholine (DMPC) was purchased from Avanti Polar Lipids Inc. (AL, USA). Cholesteryl oleate was obtained from Sigma-Aldrich Co. (MO, USA). 1,1′-Dioctadecyl-3,3,3′,3′-tetramethylindotricarbocyanine iodide bis-oleate (DiR-BOA) and the (*Z*)-octadec-9-enyl 2-(3-((*Z*)-octadec-9-enyloxy)-6-oxo-6*H*-xanthen-9-yl) benzoate was synthesized by the previously reported methods.[32] The ApoA-1 mimetic R4F peptide, Ac-FAEKFKEAVKDYFAKFWD, was purchased from GL Biochem Ltd. (Shanghai, China). Porphyrin-lipid was synthesized by the previously reported methods.[14]

PLP Preparation and Characterization. PLP lipid film consists of 0.9 μmol porphyrin-lipid, 2.1 μmol DMPC and 0.3 μmol cholesteryl oleate was prepared under a stream of nitrogen gas. For DiR-BOA-loaded particles, a 3 mol % DiR-BOA was included in the lipid film. For PEGylated PLP formulation, 5 mol % DSPE-PEG_{2000} was added in the lipid film preparation. The completely dried lipid films were hydrated with 1.0 mL of PBS buffer (150 mM, pH 7.5) and sonicated using Bioruptor at low frequency (30 kHz) for 30 cycles (30 s on/30 s off) at 40 °C. R4F peptide (2.3 mg) in 1 mL of PBS was then added into the rehydrated solution and the mixture was kept shaking at 4 °C overnight. The solution was centrifuged at 12 000 rpm for 20 min subsequently and filtered with 0.1 μm membrane (Millex, Sigma-Aldrich). ^{64}Cu-PLP was synthesized using the method reported previously.[65] Briefly, PLP was 1:1 diluted with 0.1 M NH_4OAC buffer (pH 5.5), and then mixed with $^{64}CuCl_2$ solution and incubating at 37 °C for 60 min. Small aliquot of the mixture was purified with the centrifugal units (30K, Amicon Ultra) and the radiochemical purity and yield were assessed.

The prepared PLP was subjected to TEM scanning and dynamic light scattering measurement to determine the particle morphology and size distribution. In the photoproperties measurement, PLP was diluted in either PBS (intact particles) or PBS containing 0.5% Triton X-100 (nanostructure disrupted sample), and subjected to the circular dichroism spectrum, absorption spectra and fluorescence spectrum measurement. Singlet oxygen ($^1O_2$) generation of PLP were measured using singlet oxygen sensor green (SOSG) assay. For the blood clearance study in mice, PLP (n = 5), PEG−PLP (n = 5) and PLP formulation without R4F peptide (n = 4) were intravenously injected to healthy BALB/c mice at the dose of 2.5 mg/kg. Blood was collected prior to and after the injection, the fluorescence of the extracted serum was measured, and the porphyrin amount at each time point was then analyzed by Graphpad Prism to calculate half-life of the particles.

Activation of PLP *versus* Porphysome. To compare the cellular uptake of PLP *versus* porphysome, a quantitative cellular uptake study was performed by measuring the porphyrin fluorescence in cell lysate after 3 h incubation. Confocal imaging was also conducted to monitor the porphyrin fluorescence activation over time *in vitro*. To compare the fluorescence activation *in vivo*, SKOV3 tumor-bearing mice (n = 3) were intravenously injected with ^{64}Cu-PLP or ^{64}Cu-porphyroms. At 24 h after injection, the biodistribution was determined by γ-counting and tumors from both sides of the ovaries were harvested and subjected to *ex vivo* fluorescence imaging. To compare the photodynamic activation, KB-xenograft mice received PLP or porphysome injections at a dose of 5 mg/kg (n = 3 for each group) were subjected to laser irradiation (671 nm, 75 J/cm^2) at 24 h postinjection. Temperature increase of tumors during treatment was monitored by an infrared thermal camera. The therapeutic efficacy was investigated by histological analysis.

Theranostic Application of PLP on GBM Model. The accumulation and activation of PLP in glioma mice were investigated on 9L^{luc} gliosarcoma mice and compared with those of porphysomes. Bioluminescence and open-skull fluorescence imaging were acquired at 24 h after injection. To investigate the drug delivery, U87 mice were injected with DiR-BOA loaded PLP, PLP(DiR-BOA), intravenously and subjected to fluorescence imaging. Fluorescence images were performed using CRI Maestro hyperspectral imaging system with the crania opening to acquire porphyrin and DiR-BOA signals, respectively, using the filter pairs of 575−605 nm excitation/645−730 nm emission and 725−755 nm excitation/780 nm long-pass emission. *In vivo* confocal microscopic imaging was further conducted.

To evaluate the competency of PLP for fluorescence-guided surgery, orthotopic U87^{GFP} glioma mice with deep-seeded tumor were administrated with PLP(DiR-BOA) intravenously. The mice were scarified at 24 h postinjection and the entire brains were subjected to FMT imaging. Following the brain transection procedure illustrated in Figure 4d, the two transected portions were subjected to fluorescence imaging using Maestro system to acquire the signal of GFP, porphyrin and DiR-BOA using different filter pairs (the filter pair for tumor GFP signal is 445−490 nm excitation/515−550 nm emission).

For multifoci resection, *ex vivo* bioluminescence imaging and fluorescence imaging were performed on all the resected U87^{luc} tumors and the remained surgery bed of brain.

The PDT efficacy of PLP for glioma treatment was evaluated on the U87^{luc} mice. The mice were categorized into four groups: blank control group, PDT laser alone, PLP injection alone and PLP−PDT (PLP injection plus PDT laser treatment) ($n = 3$ for each group). The PLP was dosed intravenously at 5 mg/kg and the 671 nm laser irradiation was performed at 24 h postinjection in the trans-cranium manner with laser intensity of 50 mW/cm^2 and total light dose of 50 J/cm^2. The therapeutic efficacy was evaluated by histological analysis.

Multimodal Imaging and Biodistribution Studies of ^{64}Cu-PLP in Orthotopic and Metastatic Cancer Mouse Models. To study the specific uptake of PLP in orthotopic cancer, PC-3 orthotopic prostate tumor-bearing mice were injected with ^{64}Cu-PLP and subjected to PET/CT scanning at 24 h postinjection ($n = 5$). Animals were sacrificed after the scanning, tumor and surrounding organs were then harvested and subjected to fluorescence imaging. After the *ex vivo* imaging, organs of interest were weighed and subjected to the radioactivity measurement by γ-counting assay to calculate the PLP distribution as percentage of the injected dose per gram (% ID/g). For FMT/CT imaging, mice received 10 mg/kg of PLP were subjected sequentially to FMT imaging and microCT scanning in the same chamber at 24 h postinjection. The 3D images from FMT and micro-CT were coregistered using Inveon Research Workplace. For metastatic tumor imaging, MT-1^{luc} metastatic mouse model that received ^{64}Cu-PLP injection was subjected to PET/CT scanning at 24 h postinjection. The mice were then scarified, and the metastatic tumor and surrounding tissues were subjected to *ex vivo* bioluminescence and fluorescence imaging. The metastases were further affirmed by histology studies.

Conflict of Interest: The authors declare no competing financial interest.

Acknowledgment. The authors are thankful for funding support from the Canadian Institutes of Health Research, Ontario Institute for Cancer Research, Natural Sciences and Engineering Research Council of Canada, Major International (Regional) Joint Research Project from National Science Foundation of China, US Army Ovarian Cancer Research Program Translational Synergistic Leverage Award, Prostate Cancer Canada, Canada Foundation for Innovation, Princess Margaret Cancer Foundation and the Joey and Toby Tanenbaum/Brazilian Ball Chair in Prostate Cancer Research. L.C., J.C. and G.Z. conceived the project, planned the experiment, interpreted the data and wrote the manuscript. L.C., Q.L. and J.C. developed and characterized the formulations. L.C. and C.S.J. carried out phototherapy procedures and biodistrubtion studies. W.J. and L.D set up animal models and assisted L.C. in the experiments conducted in GBM models. L.C. and H.H. carried out FMT/CT and PET/CT imaging studies. N.M, J.C.I. and F.W. contributed in the manuscript editing.

Supporting Information Available: Method description in details; The size distribution of PLP (Figure S1); The characterization of PLP containing different molar percentage of porphyrin-lipid (Figure S2); The phototoxicity of PLP−PDT treatment to glioma mice (Figure S3); The characterization of the drug loaded PLP(DiR-BOA) (Figure S4); The biodistribution of PLP(DiR-BOA) in glioma tumor and major organs (Figure S5); The uptake of PLP in sham control (Figure S6); The tissue histology analysis after PLP fluorescence-guided glioma tumor resection (Figure S7); Representative MRI images of orthotopic prostate and ovarian cancer model (Figure S8). This material is available free of charge *via* the Internet at http://pubs.acs.org.

REFERENCES AND NOTES

1. Maeda, H.; Wu, J.; Sawa, T.; Matsumura, Y.; Hori, K. Tumor Vascular Permeability and the Epr Effect in Macromolecular Therapeutics: A Review. *J. Controlled Release* **2000**, *65*, 271–284.
2. Liu, J.; Bu, W.; Pan, L.; Shi, J. NiR-Triggered Anticancer Drug Delivery by Upconverting Nanoparticles with Integrated Azobenzene-Modified Mesoporous Silica. *Angew. Chem., Int. Ed. Engl.* **2013**, *52*, 4375–4379.
3. Xie, J.; Xu, C.; Kohler, N.; Hou, Y.; Sun, S. Controlled Pegylation of Monodisperse Fe_3O_4 Nanoparticles for Reduced Non-Specific Uptake by Macrophage Cells. *Adv. Mater.* **2007**, *19*, 3163–3166.
4. Wuelfing, W. P.; Gross, S. M.; Miles, D. T.; Murray, R. W. Nanometer Gold Clusters Protected by Surface-Bound Monolayers of Thiolated Poly(Ethylene Glycol) Polymer Electrolyte. *J. Am. Chem. Soc.* **1998**, *120*, 12696–12697.
5. Maltzahn, G.; Park, J.; Agrawal, A.; Bandaru, N. K.; Das, S. K.; Sailor, M. J.; Bhatia, S. N. Computationally Guided Photothermal Tumor Therapy Using Long-Circulating Gold Nanorod Antennas. *Cancer Res.* **2009**, *69*, 3892–3900.
6. Qian, X.; Peng, X.; Ansari, D. O.; Yin-Goen, Q.; Chen, G. Z.; Shin, D. M.; Yang, L.; Young, A. N.; Wang, M. D.; Nie, S. *In Vivo* Tumor Targeting and Spectroscopic Detection with Surface-Enhanced Raman Nanoparticle Tags. *Nat. Biotechnol.* **2008**, *26*, 83–90.
7. Koole, R.; van Schooneveld, M. M.; Hilhorst, J.; Castermans, K.; Cormode, D. P.; Strijkers, G. J.; de Mello Donegá, C.; Vanmaekelbergh, D.; Griffioen, A. W.; Nicolay, K.; *et al.* Paramagnetic Lipid-Coated Silica Nanoparticles with a Fluorescent Quantum Dot Core: A New Contrast Agent Platform for Multimodality Imaging. *Bioconjugate Chem.* **2008**, *19*, 2471–2479.
8. Yoon, T.; Yu, K.; Kim, E.; Kim, J.; Kim, B.; Yun, S.; Sohn, B.; Cho, M.; Lee, J.; Park, S. Specific Targeting, Cell Sorting, and Bioimaging with Smart Magnetic Silica Core−Shell Nanomaterials. *Small* **2006**, *2*, 209–215.
9. Liu, J.; Yu, M.; Ning, X.; Zhou, C.; Yang, S.; Zheng, J. Pegylation and Zwitterionization: Pros and Cons in the Renal Clearance and Tumor Targeting of Near-IR-Emitting Gold Nanoparticles. *Angew. Chem., Int. Ed. Engl.* **2013**, *52*, 12572–12576.
10. Gref, R.; Minamitake, Y.; Peracchia, M. T.; Trubetskoy, V.; Torchilin, V.; Langer, R. Biodegradable Long-Circulating Polymeric Nanospheres. *Science* **1994**, *263*, 1600–1603.
11. Park, J. Liposome-Based Drug Delivery in Breast Cancer Treatment. *Breast Cancer Res.* **2002**, *4*, 95–99.
12. Peracchia, M. T.; Fattal, E.; Desmaële, D.; Besnard, M.; Noël, J. P.; Gomis, J. M.; Appel, M.; d'Angelo, J.; Couvreur, P. Stealth® Pegylated Polycyanoacrylate Nanoparticles for Intravenous Administration and Splenic Targeting. *J. Controlled Release* **1999**, *60*, 121–128.
13. Otsuka, H.; Nagasaki, Y.; Kataoka, K. Pegylated Nanoparticles for Biological and Pharmaceutical Applications. *Adv. Drug Delivery Rev.* **2003**, *55*, 403–419.
14. Lovell, J. F.; Jin, C. S.; Huynh, E.; Jin, H.; Kim, C.; Rubinstein, J. L.; Chan, W. C.; Cao, W.; Wang, L. V.; Zheng, G. Porphysome Nanovesicles Generated by Porphyrin Bilayers for Use as Multimodal Biophotonic Contrast Agents. *Nat. Mater.* **2011**, *10*, 324–332.
15. Amoozgar, Z.; Yeo, Y. Recent Advances in Stealth Coating of Nanoparticle Drug Delivery Systems. *Wiley Interdiscip. Rev.: Nanomed. Nanobiotechnol.* **2012**, *4*, 219–233.
16. Mishra, S.; Webster, P.; Davis, M. E. Pegylation Significantly Affects Cellular Uptake and Intracellular Trafficking of Non-Viral Gene Delivery Particles. *Eur. J. Cell Biol.* **2004**, *83*, 97–111.
17. Hatakeyama, H.; Akita, H.; Harashima, H. A Multifunctional Envelope Type Nano Device (Mend) for Gene Delivery to Tumours Based on the Epr Effect: A Strategy for Overcoming the Peg Dilemma. *Adv. Drug Delivery Rev.* **2011**, *63*, 152–160.
18. Hong, R.; Huang, C.; Tseng, Y.; Pang, V.; Chen, S.; Liu, J.; Chang, F. Direct Comparison of Liposomal Doxorubicin with or without Polyethylene Glycol Coating in C-26 Tumor-Bearing Mice: Is Surface Coating with Polyethylene Glycol Beneficial? *Clin. Cancer Res.* **1999**, *5*, 3645–3652.
19. Moghimi, S. M.; Hamad, I.; Andresen, T. L.; Jørgensen, K.; Szebeni, J. Methylation of the Phosphate Oxygen Moiety of Phospholipid-Methoxy(Polyethylene Glycol) Conjugate

Prevents Pegylated Liposome-Mediated Complement Activation and Anaphylatoxin Production. *FASEB J.* **2006**, *20*, 2591–2593.
20. Hamad, I.; Hunter, A. C.; Szebeni, J.; Moghimi, S. M. Poly-(Ethylene Glycol)s Generate Complement Activation Products in Human Serum through Increased Alternative Pathway Turnover and a MASP-2-Dependent Process. *Mol. Immunol.* **2008**, *46*, 225–232.
21. Ishida, T.; Maeda, R.; Ichihara, M.; Irimura, K.; Kiwada, H. Accelerated Clearance of Pegylated Liposomes in Rats after Repeated Injections. *J. Controlled Release* **2003**, *88*, 35–42.
22. Ishida, T.; Ichihara, M.; Wang, X.; Yamamoto, K.; Kimura, J.; Majima, E.; Kiwada, H. Injection of PEGylated Liposomes in Rats Elicits PEG-Specific Igm, Which Is Responsible for Rapid Elimination of a Second Dose of PEGylated Liposomes. *J. Controlled Release* **2006**, *112*, 15–25.
23. Dams, E. T. M.; Laverman, P.; Oyen, W. J. G.; Storm, G.; Scherphof, G. L.; van der Meer, J. W. M.; Corstens, F. H. M.; Boerman, O. C. Accelerated Blood Clearance and Altered Biodistribution of Repeated Injections of Sterically Stabilized Liposomes. *J. Pharmacol. Exp. Ther.* **2000**, *292*, 1071–1079.
24. Robert, N. J.; Vogel, C. L.; Henderson, I. C.; Sparano, J. A.; Moore, M. R.; Silverman, P.; Overmoyer, B. A.; Shapiro, C. L.; Park, J. W.; Colbern, G. T.; *et al.* The Role of the Liposomal Anthracyclines and Other Systemic Therapies in the Management of Advanced Breast Cancer. *Semin. Oncol.* **2004**, *31*, 106–146.
25. Duncan, R.; Gaspar, R. Nanomedicine(s) under the Microscope. *Mol. Pharmaceutics* **2011**, *8*, 2101–2141.
26. MacEwan, S. R.; Callahan, D. J.; Chilkoti, A. Stimulus-Responsive Macromolecules and Nanoparticles for Cancer Drug Delivery. *Nanomedicine* **2010**, *5*, 793–806.
27. Vllasaliu, D.; Fowler, R.; Stolnik, S. Pegylated Nanomedicines: Recent Progress and Remaining Concerns. *Expert Opin. Drug Delivery* **2014**, *11*, 139–154.
28. Chambers, E.; Mitragotri, S. Prolonged Circulation of Large Polymeric Nanoparticles by Non-Covalent Adsorption on Erythrocytes. *J. Controlled Release* **2004**, *100*, 111–119.
29. Eisenberg, S.; Windmueller, H. G.; Levy, R. I. Metabolic Fate of Rat and Human Lipoprotein Apoproteins in the Rat. *J. Lipid Res.* **1973**, *14*, 446–458.
30. Ng, K. K.; Lovell, J. F.; Zheng, G. Lipoprotein-Inspired Nanoparticles for Cancer Theranostics. *Acc. Chem. Res.* **2011**, *44*, 1105–1113.
31. Corbin, I. R.; Zheng, G. Mimicking Nature's Nanocarrier: Synthetic Low-Density Lipoprotein-Like Nanoparticles for Cancer-Drug Delivery. *Nanomedicine* **2007**, *2*, 375–380.
32. Zhang, Z.; Cao, W.; Jin, H.; Lovell, J. F.; Yang, M.; Ding, L.; Chen, J.; Corbin, I.; Luo, Q.; Zheng, G. Biomimetic Nanocarrier for Direct Cytosolic Drug Delivery. *Angew. Chem., Int. Ed. Engl.* **2009**, *48*, 9171–9175.
33. Cormode, D. P.; Frias, J. C.; Ma, Y.; Chen, W.; Skajaa, T.; Briley-Saebo, K.; Barazza, A.; Williams, K. J.; Mulder, W. J.; Fayad, Z. A.; Fisher, E. A. HDL as a Contrast Agent for Medical Imaging. *Clin. Lipidol.* **2009**, *4*, 493–500.
34. Bricarello, D. A.; Smilowitz, J. T.; Zivkovic, A. M.; German, J. B.; Parikh, A. N. Reconstituted Lipoprotein: A Versatile Class of Biologically-Inspired Nanostructures. *ACS Nano* **2011**, *5*, 42–57.
35. Huang, H.; Cruz, W.; Chen, J.; Zheng, G. Learning from Biology: Synthetic Lipoproteins for Drug Delivery. *Wiley Interdiscip. Rev.: Nanomed. Nanobiotechnol.* **2014**, 10.1002/wnan.1308.
36. Marrache, S.; Dhar, S. Biodegradable Synthetic High-Density Lipoprotein Nanoparticles for Atherosclerosis. *Proc. Natl. Acad. Sci. U. S. A.* **2013**, *110*, 9445–9450.
37. Foit, L.; Giles, F. J.; Gordon, L. I.; Thaxton, C. S. Synthetic High-Density Lipoprotein-Like Nanoparticles for Cancer Therapy. *Expert Rev. Anticancer Ther.* **2015**, *15*, 27–34.
38. Allijn, I. E.; Leong, W.; Tang, J.; Gianella, A.; Mieszawska, A. J.; Fay, F.; Ma, G.; Russell, S.; Callo, C. B.; Gordon, R. E.; *et al.* Gold Nanocrystal Labeling Allows Low-Density Lipoprotein Imaging from the Subcellular to Macroscopic Level. *ACS Nano* **2013**, *7*, 9761–9770.
39. Cormode, D. P.; Skajaa, T.; van Schooneveld, M. M.; Koole, R.; Jarzyna, P.; Lobatto, M. E.; Calcagno, C.; Barazza, A.; Gordon, R. E.; Zanzonico, P.; *et al.* Nanocrystal Core High-Density Lipoproteins: A Multimodality Contrast Agent Platform. *Nano Lett.* **2008**, *8*, 3715–3723.
40. Saxena, V. P.; Wetlaufer, D. B. A New Basis for Interpreting the Circular Dichroic Spectra of Proteins. *Proc. Natl. Acad. Sci. U. S. A.* **1971**, *68*, 969–972.
41. Zhang, Z.; Chen, J.; Ding, L.; Jin, H.; Lovell, J. F.; Corbin, I. R.; Cao, W.; Lo, P. C.; Yang, M.; Tsao, M. S.; *et al.* HDL-Mimicking Peptide-Lipid Nanoparticles with Improved Tumor Targeting. *Small* **2010**, *6*, 430–437.
42. Jin, C. S.; Lovell, J. F.; Chen, J.; Zheng, G. Ablation of Hypoxic Tumors with Dose-Equivalent Photothermal, but Not Photodynamic, Therapy Using a Nanostructured Porphyrin Assembly. *ACS Nano* **2013**, *7*, 2541–2550.
43. Zhan, C.; Lu, W. The Blood-Brain/Tumor Barriers: Challenges and Chances for Malignant Gliomas Targeted Drug Delivery. *Curr. Pharm. Biotechnol.* **2012**, *13*, 2380–2387.
44. Stukel, J. M.; Caplan, M. R. Targeted Drug Delivery for Treatment and Imaging of Glioblastoma Multiforme. *Expert Opin. Drug Delivery* **2009**, *6*, 705–718.
45. Bechet, D.; Mordon, S. R.; Guillemin, F.; Barberi-Heyob, M. A. Photodynamic Therapy of Malignant Brain Tumours: A Complementary Approach to Conventional Therapies. *Cancer Treat. Rev.* **2014**, *40*, 229–241.
46. Muller, P. J.; Wilson, B. C. Photodynamic Therapy of Brain Tumors—a Work in Progress. *Lasers Surg. Med.* **2006**, *38*, 384–389.
47. Wilson, T. A.; Karajannis, M. A.; Harter, D. H. Glioblastoma Multiforme: State of the Art and Future Therapeutics. *Surg. Neurol. Int.* **2014**, *5*, 64.
48. Eyupoglu, I. Y.; Buchfelder, M.; Savaskan, N. E. Surgical Resection of Malignant Gliomas-Role in Optimizing Patient Outcome. *Nat. Rev. Neurol.* **2013**, *9*, 141–151.
49. Hassaneen, W.; Levine, N. B.; Suki, D.; Salaskar, A. L.; de Moura Lima, A.; McCutcheon, I. E.; Prabhu, S. S.; Lang, F. F.; DeMonte, F.; Rao, G.; *et al.* Multiple Craniotomies in the Management of Multifocal and Multicentric Glioblastoma. Clinical Article. *J. Neurosurg.* **2011**, *114*, 576–584.
50. MacDonald, T. D.; Liu, T. W.; Zheng, G. An MRI-Sensitive, Non-Photobleachable Porphysome Photothermal Agent. *Angew. Chem., Int. Ed. Engl.* **2014**, *53*, 6956–6959.
51. Lin, Q.; Chen, J.; Jin, H.; Ng, K. K.; Yang, M.; Cao, W.; Ding, L.; Zhang, Z.; Zheng, G. Efficient Systemic Delivery of Sirna by Using High-Density Lipoprotein-Mimicking Peptide Lipid Nanoparticles. *Nanomedicine* **2012**, *7*, 1813–1825.
52. Lin, Q.; Chen, J.; Zhang, Z.; Zheng, G. Lipid-Based Nanoparticles in the Systemic Delivery of Sirna. *Nanomedicine* **2014**, *9*, 105–120.
53. Shahzad, M. M.; Mangala, L. S.; Han, H. D.; Lu, C.; Bottsford-Miller, J.; Nishimura, M.; Mora, E. M.; Lee, J. W.; Stone, R. L.; Pecot, C. V.; *et al.* Targeted Delivery of Small Interfering Rna Using Reconstituted High-Density Lipoprotein Nanoparticles. *Neoplasia* **2011**, *13*, 309–319.
54. Rui, M.; Tang, H.; Li, Y.; Wei, X.; Xu, Y. Recombinant High Density Lipoprotein Nanoparticles for Target-Specific Delivery of Sirna. *Pharm. Res.* **2013**, *30*, 1203–1214.
55. McConathy, W. J.; Nair, M. P.; Paranjape, S.; Mooberry, L.; Lacko, A. G. Evaluation of Synthetic/Reconstituted High-Density Lipoproteins as Delivery Vehicles for Paclitaxel. *Anti-Cancer Drugs* **2008**, *19*, 183–188.
56. Yang, M.; Chen, J.; Cao, W.; Ding, L.; Ng, K. K.; Jin, H.; Zhang, Z.; Zheng, G. Attenuation of Nontargeted Cell-Kill Using a High-Density Lipoprotein-Mimicking Peptide−Phospholipid Nanoscaffold. *Nanomedicine* **2011**, *6*, 631–641.
57. Duivenvoorden, R.; Tang, J.; Cormode, D. P.; Mieszawska, A. J.; Izquierdo-Garcia, D.; Ozcan, C.; Otten, M. J.; Zaidi, N.; Lobatto, M. E.; van Rijs, S. M.; *et al.* A Statin-Loaded Reconstituted High-Density Lipoprotein Nanoparticle Inhibits Atherosclerotic Plaque Inflammation. *Nat. Commun.* **2014**, *5*, 3065.
58. Jin, C. S.; Cui, L.; Wang, F.; Chen, J.; Zheng, G. Targeting-Triggered Porphysome Nanostructure Disruption for Activatable Photodynamic Therapy. *Adv. Healthcare Mater.* **2014**, *3*, 1240–1249.

59. Perrault, S. D.; Walkey, C.; Jennings, T.; Fischer, H. C.; Chan, W. C. Mediating Tumor Targeting Efficiency of Nanoparticles through Design. *Nano Lett.* **2009**, *9*, 1909–1915.
60. Cabral, H.; Matsumoto, Y.; Mizuno, K.; Chen, Q.; Murakami, M.; Kimura, M.; Terada, Y.; Kano, M. R.; Miyazono, K.; Uesaka, M.; Nishiyama, N.; Kataoka, K. Accumulation of Sub-100 nm Polymeric Micelles in Poorly Permeable Tumours Depends on Size. *Nat. Nanotechnol.* **2011**, *6*, 815–823.
61. Yuan, F.; Leunig, M.; Huang, S. K.; Berk, D. A.; Papahadjopoulos, D.; Jain, R. K. Microvascular Permeability and Interstitial Penetration of Sterically Stabilized (Stealth) Liposomes in a Human Tumor Xenograft. *Cancer Res.* **1994**, *54*, 3352–3356.
62. Davis, M. E.; Chen, Z. G.; Shin, D. M. Nanoparticle Therapeutics: An Emerging Treatment Modality for Cancer. *Nat. Rev. Drug Discovery* **2008**, *7*, 771–782.
63. Cheng, L.; Wang, C.; Feng, L.; Yang, K.; Liu, Z. Functional Nanomaterials for Phototherapies of Cancer. *Chem. Rev.* **2014**, *114*, 10869–10939.
64. Chapman, M. J. Animal Lipoproteins: Chemistry, Structure, and Comparative Aspects. *J. Lipid Res.* **1980**, *21*, 789–853.
65. Liu, T. W.; MacDonald, T.; Shi, J.; Wilson, B. C.; Zheng, G. Intrinsically Copper-64-Labeled Organic Nanoparticles as Radiotracers. *Angew. Chem., Int. Ed. Engl.* **2012**, *51*, 1–5.